

Joint growth rate measurements from redshift-space distortions and peculiar velocities in the 6dF Galaxy Survey

Caitlin Adams¹ and Chris Blake¹★

¹Centre for Astrophysics & Supercomputing, Swinburne University of Technology, P.O. Box 218, Hawthorn, VIC 3122, Australia.

Accepted XXX. Received YYY; in original form ZZZ

ABSTRACT

We present a new model for the cross-covariance between galaxy redshift-space distortions and peculiar velocities. We combine this with the auto-covariance models of both probes in a fully self-consistent, maximum-likelihood method, allowing us to extract enhanced cosmological parameter constraints. When applying our method to the 6-degree Field Galaxy Survey (6dFGS), our constraint on the growth rate of structure is $f\sigma_8 = 0.384 \pm 0.052(\text{stat}) \pm 0.061(\text{sys})$ and our constraint for the redshift-space distortion parameter is $\beta = 0.289^{+0.044}_{-0.043}(\text{stat}) \pm 0.049(\text{sys})$. We find that the statistical uncertainty for the growth rate of structure is reduced by 64% when using the complete covariance model compared to the redshift-space distortion auto-covariance model and 50% when compared to using the peculiar velocity auto-covariance model. Our constraints are consistent with those from the literature on combining multiple tracers of large-scale structure, as well as those from other 6dFGS analyses. Our measurement is also consistent with the standard cosmological model.

Key words: surveys, cosmology: observations, cosmological parameters, large-scale structure of Universe

1 INTRODUCTION

The current cosmological model explains the observed accelerating expansion of the Universe by including a dark energy component in Einstein’s general relativistic field equations. While this model is supported by numerous high- and low-redshift observations, such as the cosmic microwave background (CMB; e.g. Planck Collaboration et al. 2018), baryon acoustic oscillations (BAO; e.g. Ata et al. 2018) and type Ia supernovae (SNe Ia; e.g. Scolnic et al. 2017), we have a poor understanding of the physical nature of dark energy. A possible alternative theory for the accelerating expansion would be that gravity behaves differently on cosmological scales, generally classed as modified gravity theories. However, we require higher precision tests on large scales if we are to distinguish between dark energy and modified gravity.

Modifying gravity directly affects how structures like galaxies and galaxy clusters form in the Universe. Therefore, one of the key ways we can test gravity on large scales is through the linear growth rate of structure, $f(a) \equiv d \ln(D(a))/d \ln(a)$, where D is the linear growth function describing the growth of matter perturbations and a is the scale factor, which characterises the Universe’s expansion.

General relativity predicts that the value of the growth rate should be a function of the total matter density through $f(a) \approx \Omega_m(a)^{0.55}$ (Linder 2005). Precise measurements of the growth rate may help to rule out dark energy or alternative models.

The growth rate of structure can be constrained by two key cosmological probes: direct measurements of peculiar velocities and statistical redshift space distortions. A galaxy’s peculiar velocity is its motion due to gravitational attraction, rather than its motion due to cosmological expansion. A galaxy’s total motion can be inferred from its redshift, and the peculiar velocity contribution may be extracted if one has a redshift-independent distance measure of the galaxy’s position, such as through the Fundamental Plane or Tully-Fisher methods. Importantly, peculiar velocities are directly proportional to the underlying matter overdensity field via the growth rate, and at linear scales, peculiar velocities are considered to be unbiased tracers of the matter overdensity field (Desjacques & Sheth 2010). Because of their contribution to a galaxy’s total redshift, peculiar velocities are also statistically encoded in the distribution of large-scale structure in redshift space, a signal known as the redshift-space distortion (RSD). Originally modelled by Kaiser (1987), redshift-space distortions allow us to also constrain the growth rate of structure without requiring a

★ E-mail: cblake@swin.edu.au

redshift-independent distance estimator. RSD studies have constrained the growth rate at the level of 10% at low redshifts ($z < 2$) (e.g. [Blake et al. 2011](#); [Beutler et al. 2012](#); [Alam et al. 2017](#); [Ruggeri et al. 2019](#)).

Peculiar velocities and redshift-space distortions constrain the growth rate on different physical scales; peculiar velocities are sensitive to the underlying matter overdensity field on scales of hundreds of h^{-1} Mpc, where redshift-space distortions are sensitive on scales of tens of h^{-1} Mpc. This makes them highly-complementary when it comes to constraining the growth rate. One way to take advantage of this complementarity is through density-velocity comparison methods, which use gravitational instability theory to predict one field from the other, then constrain the ratio of the growth rate and galaxy bias $\beta \equiv f/b$ by comparing the predicted and observed fields (e.g. [Pike & Hudson 2005](#); [Davis et al. 2011](#); [Carrick et al. 2015](#)). Multiple works have also shown that combining correlated tracers of the matter overdensity field leads to improved constraints on cosmological parameters (e.g. [McDonald & Seljak 2009](#); [Gil-Marín et al. 2010](#); [Bernstein & Cai 2011](#); [Abramo & Leonard 2013](#); [Blake et al. 2013](#)). [Adams & Blake \(2017\)](#) demonstrated that this effect extends to combining peculiar velocities and galaxy overdensities; by utilising the cross-correlation of these probes, they were able to improve the constraint on the growth rate by $\sim 20\%$ compared to treating the probes independently.

This study builds upon two existing works: that of [Johnson et al. \(2014\)](#), who constrained the growth rate of structure by modelling the peculiar velocity auto-correlation; and that of [Adams & Blake \(2017\)](#), who constrained the growth rate by modelling the cross-correlation between the galaxy overdensity and peculiar velocity fields, in addition to their auto-correlations. We note that [Adams & Blake \(2017\)](#) did not include a complete model of redshift-space distortions, meaning the galaxy overdensity field was only a function of the linear galaxy bias. In this study, we aim to update the model to include a fully self-consistent description of redshift-space distortions, meaning that the galaxy overdensity field is a function of the linear galaxy bias and the growth rate of structure. We hypothesise that this will provide tighter constraints on the growth rate of structure, due to the complementary information provided by redshift-space distortions and peculiar velocities. We validate our model by applying it to mock catalogues that are significantly more sophisticated than those utilised by [Adams & Blake \(2017\)](#); we then apply our analysis to data from the 6-degree Field Galaxy Survey (6dFGS). We also extend the work by [Adams & Blake \(2017\)](#) by conducting a thorough analysis of the model systematics, including the calculation of a systematic uncertainty contribution to our growth rate of structure constraint.

We begin by introducing the data and simulations in Section 2. We discuss the theory and methodology in Section 3. The results from our tests on simulations are given in Section 4, followed by those from the 6dFGS data in Section 5. Finally, we conclude with a summary in Section 6.

2 DATA AND SIMULATIONS

We use measurements of the galaxy overdensity and peculiar velocity field from galaxy redshift surveys to constrain the growth rate of structure. In this section, we cover the observed and simulated data used in our analysis.

2.1 6dFGS

We utilise data from the 6-degree Field Galaxy Survey (6dFGS; [Jones et al. 2005, 2006, 2009](#)). Conducted on the UK Schmidt Telescope, the survey covers the southern sky (excluding 10 degrees around the galactic plane) out to redshift $z \approx 0.23$. The survey consists of two key samples: the redshift sample, 6dFGSz, and the peculiar velocity sample, 6dFGSv; we work with both in this analysis.

As of the survey’s completion, 6dFGSz contains 125,071 redshifts, with a median redshift of $z = 0.053$. We draw our galaxy redshift sample from that used in the 6dFGS baryon acoustic oscillation analysis by [Beutler et al. \(2011\)](#), which selected galaxies from 6dFGSz that had magnitude $K \leq 12.9$ in sky regions with greater than 60% completeness, producing a total of 75,117 galaxies. We impose an additional selection in limiting the redshift range to be $z \leq 0.1$, leaving us with 70,467 galaxies. This restriction allows us to extract the redshift-space distortion signal in the data while balancing the computational requirements of our method, which scale with sample volume.

It is important to note that our galaxy overdensity sample is not volume-limited, which means the galaxy bias of the sample will evolve with redshift. As in previous redshift-space distortion studies (e.g. [Beutler et al. 2012](#)), we may conveniently model the sample as having a single effective bias over the whole redshift range. We note that this has some consequences for our modelling of the cross-correlation between the peculiar velocity and galaxy overdensity field, which may sample a different effective galaxy bias to the galaxy overdensity field; we discuss the evidence and proposed model for this effect in Section 3.3.4.

The final 6dFGSv sample consists of 9794 Fundamental Plane measurements in the redshift range $z \leq 0.057$, with distance errors of around 26% ([Magoulas et al. 2012](#)). We use the sample as defined by [Springob et al. \(2014\)](#), who selected galaxies with signal-to-noise ratios of greater than 5Å^{-1} , and velocity dispersions greater than the resolution limit of the 6dF spectrograph ($\sigma_0 \geq 112\text{km s}^{-1}$). This selection yielded logarithmic distance ratios for 8,885 galaxies, where the logarithmic distance ratio η is related to the peculiar velocity v_p , but is preferred because of its Gaussian distribution (see [Johnson et al. 2014](#)).

As in [Adams & Blake \(2017\)](#), we grid our galaxy redshift and logarithmic distance ratio samples, which allows us to simultaneously smooth over non-linear effects and reduce the computational requirements of our analysis (see Section 3.3.2). We used a gridding scale of $L_\delta = 30 h^{-1}$ Mpc for the galaxy redshift sample, and a gridding scale of $L_\eta = 20 h^{-1}$ Mpc for the logarithmic distance ratio sample. This resulted in $N_\delta = 1633$ grid cells for our redshift sample, and $N_\eta = 908$ grid cells for our logarithmic distance ratio sample.

Gridding the redshift sample allows us to directly calculate the galaxy overdensity in each cell by comparing the

number of galaxies in the cell N_{cell} to the number expected for the cell N_{exp} through $\delta_g = \frac{N_{\text{cell}}}{N_{\text{exp}}} - 1$. We estimated N_{exp} from the survey selection function, which we generated by combining the survey luminosity function with the position-dependent magnitude completeness (Jones et al. 2006). These values were then normalised so that the total N_{exp} value matched the total number of galaxies in our redshift sample and used to calculate the overdensity. The shot noise for each galaxy overdensity measurement is determined from Poisson statistics as $\sigma_{\delta_g} = 1/\sqrt{N_{\text{exp}}}$.

We calculate the logarithmic distance ratio measurement for each cell as the average of all measurements within that cell. The observational uncertainties are added in quadrature, giving an error in the mean. We refer the reader to Abate et al. (2008) for the motivation behind this approach, and note that we discuss how it affects the modelling of the logarithmic distance ratio auto-covariance in Section 3.3.2.

2.2 Simulations

We use the data and random mock catalogues developed by Carter et al. (2018), which include accurate modelling of the halo occupation distribution of 6dFGS. Each mock is drawn from a unique COMoving Lagrangian Acceleration (COLA; Tashev et al. 2013) simulation, where each simulation has a box-length of $1.2 h^{-1} \text{Gpc}$ and contains $(1728)^3$ particles with a mass resolution of $2.8 \times 10^{10} h^{-1} M_{\odot}$. The advantage in using the COLA method is that it is faster than standard N-body techniques; the speed-gain comes from sacrificing accuracy on small scales, while retaining accuracy on large scales by exactly solving the linear perturbation theory equations. The fiducial cosmology used to generate the simulations is listed as the first column in Table 1.

The mock catalogues were generated by taking a simulation snapshot at redshift $z = 0.1$ (close to the effective redshift of 6dFGS) and populating it using a halo occupation distribution (HOD) model. The HOD is informed by the number density function $n(z)$ and projected correlation function $w_p(r_p)$ of 6dFGS, and allocates both central and satellite galaxies to the N-body halos. The random catalogues were populated by drawing Monte Carlo samples from the 6dFGS selection function, which accounts for both the angular and redshift distribution of galaxies in the survey. We apply our method to ten mock catalogues, which helps us assess the reliability of our method.

We take several additional steps to refine the ten mocks. Our logarithmic distance ratio sample is obtained by taking the 8885 most massive centrals in the 6dFGSv redshift range $z \leq 0.057$ and converting the given peculiar velocity into a logarithmic distance ratio (via Eq. 21). We add mock measurement uncertainties to the logarithmic distance ratios by first drawing a random offset η_{offset} from the normal distribution $\mathcal{N}(0, \sigma_{\text{obs}} = 0.1)$, where σ_{obs} represents the typical level of uncertainty in the 6dFGSv logarithmic distance ratios. We then modify the true logarithmic distance ratio through $\eta_{\text{modified}} = \eta_{\text{true}} + \eta_{\text{offset}}$ and set the observed uncertainty to σ_{obs} . Our galaxy overdensity sample is selected from both central and satellite galaxies below redshift $z = 0.1$ (matching the redshift limit of our 6dFGS galaxy redshift sample). When calculating the galaxy overdensities, we use a

slightly different method for calculating N_{exp} compared to the 6dFGS data, which we estimate using the average $n(z)$ function from the random catalogues associated with the mock catalogues. We did not use this method for the 6dFGS data because its angular selection function and number density function are not explicitly separable, hence the use of random catalogues determined from the luminosity function (see above). Finally, the data mock catalogues are gridded at the same length-scales as the 6dFGS data: $L_{\delta_g} = 30 h^{-1} \text{Mpc}$ and $L_{\eta} = 20 h^{-1} \text{Mpc}$.

3 THEORY AND METHODOLOGY

As this work builds on that presented by Adams & Blake (2017), we note that the interested reader may refer back to that paper for the foundational information, as well as more depth, for the following sections.

3.1 Likelihood Model

In this study, we aim to extract constraints on the growth rate of structure by modelling the auto- and cross-covariance matrices of the peculiar velocity and galaxy overdensity fields. This is primarily done by constructing and evaluating a likelihood function, which describes the probability of observing the data given our model. This then informs the posterior probability distribution when we include known information in the form of the prior through Bayes' theorem. The likelihood is a function of the data $\mathbf{\Delta}$ and the model parameters ϕ :

$$\mathcal{L} = \frac{1}{\sqrt{(2\pi)^N |\mathbf{C}(\phi)|}} \exp\left(-\frac{1}{2} \mathbf{\Delta}^T \mathbf{C}(\phi)^{-1} \mathbf{\Delta}\right), \quad (1)$$

where $\mathbf{C}(\phi)$ is the model covariance matrix and N is the length of the data vector. In this method, the data vector contains N_{δ} galaxy overdensities $\delta_g = (\delta_{g1}, \delta_{g2}, \dots, \delta_{gN_{\delta}})$, and N_v peculiar velocities $\mathbf{v}_p = (v_{p1}, v_{p2}, \dots, v_{pN_v})$, such that it has length $N = N_{\delta} + N_v$. The model covariance matrix may be expressed using four submatrices, which are the auto- and cross-covariance matrices for the galaxy overdensity and peculiar velocity measurements:

$$\mathbf{C} = \begin{pmatrix} \mathbf{C}_{\delta\delta} & \mathbf{C}_{\delta v} \\ \mathbf{C}_{v\delta} & \mathbf{C}_{vv} \end{pmatrix}. \quad (2)$$

3.2 Covariance Model

The entries of the covariance matrix are determined by modelling the correlation between any two entries of the data vector. We begin with the expressions for the galaxy overdensity and peculiar velocity fields in Fourier space.

The observed galaxy overdensity field in redshift space is modelled as

$$\tilde{\delta}_g^s(\mathbf{k}) = [b\tilde{\delta}_m(\mathbf{k}) + f\mu^2\tilde{\theta}(\mathbf{k})]D_g(k, \mu, \sigma_g), \quad (3)$$

where b is the galaxy bias in real space, δ_m is the matter overdensity field, f is the growth rate of structure, $\mu \equiv \hat{\mathbf{k}} \cdot \hat{\mathbf{d}}$ is the angle between the wavevector \mathbf{k} and the line-of-sight \mathbf{d} and θ is the velocity divergence field. The additional term

$$D_g(k, \mu, \sigma_g) = e^{-(k\mu\sigma_g)^2/2} \quad (4)$$

is the damping due to the “fingers-of-God” effect, modelled by [Peacock & Dodds \(1994\)](#). Here, σ_g is in units of h^{-1} Mpc; it characterises the strength of the damping and is related to the pairwise velocity dispersion.

The observed peculiar velocity field is modelled as

$$\tilde{v}_p(\mathbf{k}) = -iaHf\frac{\mu}{k}\tilde{\theta}(\mathbf{k})D_u(k, \sigma_u), \quad (5)$$

where i is the imaginary unit, a is the dimensionless scale factor and H is the Hubble constant in units of $h \text{ km s}^{-1} \text{ Mpc}^{-1}$. The additional term

$$D_u(k, \sigma_u) = \frac{\sin(k\sigma_u)}{k\sigma_u} \quad (6)$$

is the damping function introduced by [Koda et al. \(2014\)](#), where σ_u characterises the strength of the damping and is in units of h^{-1} Mpc.

One may obtain expressions for the correlation functions (and hence the complete model covariance), by Fourier transforming the corresponding power spectra. The anisotropic auto- and cross-power spectra for the galaxy overdensity and peculiar velocity fields are

$$P_{gg}(k, \mu) = b^2[P_{mm}(k) + 2r_g\beta\mu^2P_{m\theta}(k) + \beta^2\mu^4P_{\theta\theta}(k)]D_g^2(k, \mu, \sigma_g), \quad (7)$$

$$P_{gv}(k, \mu) = \frac{iaHfb\mu}{k}[r_gP_{m\theta}(k) + \beta\mu^2P_{\theta\theta}(k)] \quad (8)$$

$$D_g(k, \mu, \sigma_g)D_u(k, \sigma_u),$$

$$P_{vg}(k, \mu) = \frac{-iaHfb\mu}{k}[r_gP_{m\theta}(k) + \beta\mu^2P_{\theta\theta}(k)] \quad (9)$$

$$D_g(k, \mu, \sigma_g)D_u(k, \sigma_u),$$

$$P_{vv}(k, \mu) = \left(\frac{aHf\mu}{k}\right)^2 P_{\theta\theta}(k)D_u^2(k, \sigma_u). \quad (10)$$

where we have introduced the cross-correlation coefficient r_g . This parameter allows for a more detailed galaxy bias relation, and is commonly used in RSD modelling (e.g. [Dekel & Lahav 1999](#); [Burke & Taylor 2004](#); [Blake et al. 2011](#); [Koda et al. 2014](#)). It is defined such that it modifies the galaxy bias only for the galaxy-matter cross-power spectrum. Given that $\delta_m = \theta$ on linear scales, we have applied the cross-correlation coefficient to the cross-power spectrum $P_{g\theta} = bP_{m\theta}$ in our RSD equations.

Our method is structured such that we may vary two of f , b and β as free parameters. However, recomputing the entire covariance matrix model for a new set of parameters is computationally expensive. Instead, we break up each covariance such that the subsequent component matrices can be directly scaled by the free parameters. The scaled components are then summed to get the complete model covariance. We present a summary of the covariance equations below and provide the full derivation and equations for the components in [Appendix A](#).

For the galaxy overdensity auto-covariance:

$$\mathbf{C}_{\delta\delta} = \frac{b^2}{2\pi^2}(\mathbf{C}_{\delta\delta, \beta^0} + 2r_g\beta\mathbf{C}_{\delta\delta, \beta^1} + \beta^2\mathbf{C}_{\delta\delta, \beta^2}). \quad (11)$$

Each of these components may then be expressed as the Fourier transform of the corresponding power spectrum. The Fourier transform is over angle μ and wavenumber k , so we evaluate the angular component analytically using multipole expansion, where the multipole orders are given by ℓ (see

[Appendix A](#)). This leads to us expressing the components as an integral over k :

$$\mathbf{C}_{\delta\delta, \beta^0} = \int k^2 P_{mm}(k) \sum_{\ell \in 0, 2, 4} \mathbf{K}_{\delta\delta, \beta^0, \ell} dk, \quad (12)$$

$$\mathbf{C}_{\delta\delta, \beta^1} = \int k^2 P_{m\theta}(k) \sum_{\ell \in 0, 2, 4} \mathbf{K}_{\delta\delta, \beta^1, \ell} dk, \quad (13)$$

$$\mathbf{C}_{\delta\delta, \beta^2} = \int k^2 P_{\theta\theta}(k) \sum_{\ell \in 0, 2, 4} \mathbf{K}_{\delta\delta, \beta^2, \ell} dk, \quad (14)$$

where $\mathbf{K}_{\delta\delta, \beta, \ell}$ are matrices containing the integrands for each order of β and ℓ , with their functional forms expressed in [Eq. A32 to A43](#).

For the peculiar velocity auto-covariance:

$$\mathbf{C}_{vv} = \frac{(aHf)^2}{2\pi^2}(\mathbf{C}_{vv, \beta^0}), \quad (15)$$

where

$$\mathbf{C}_{vv, \beta^0} = \int P_{\theta\theta}(k)D_u^2(k, \sigma_u) \sum_{\ell \in 0, 2} \mathbf{K}_{vv, \ell} dk, \quad (16)$$

where $\mathbf{K}_{vv, \ell}$ are matrices containing the integrands for each order of ℓ , with their functional forms expressed in [Eq. A47 to A48](#).

Finally, for the cross-covariance:

$$\mathbf{C}_{v\delta} = \frac{aHfb}{2\pi^2}(r_g\mathbf{C}_{v\delta, \beta^0} + \beta\mathbf{C}_{v\delta, \beta^1}), \quad (17)$$

where

$$\mathbf{C}_{v\delta, \beta^0} = \int k P_{\theta m}(k)D_u(k, \sigma_u) \sum_{\ell \in 1, 3} \mathbf{K}_{v\delta, \beta^0, \ell} dk, \quad (18)$$

$$\mathbf{C}_{v\delta, \beta^1} = \int k P_{\theta\theta}(k)D_u(k, \sigma_u) \sum_{\ell \in 1, 3} \mathbf{K}_{v\delta, \beta^1, \ell} dk, \quad (19)$$

where $\mathbf{K}_{\delta\delta, \beta, \ell}$ are matrices containing the integrands for each order of β and ℓ , with their functional forms expressed in [Eq. A53 to A58](#).

3.3 Model Modifications

In [Adams & Blake \(2017\)](#), we introduced several modifications to the covariance model to better capture the data. We refer the reader to sections 3.3, 3.4 and 3.7 in that work, and provide a brief overview of the key modifications below.

3.3.1 Modelling the Logarithmic Distance Ratio

[Springob et al. \(2014\)](#) showed that peculiar velocities measured from 6dFGS have log-normal, rather than Gaussian, uncertainty distributions, making them unsuitable for our likelihood model. However, the use of the Fundamental Plane method in that work also allows the peculiar velocity measurements to be written as a logarithmic distance ratio, defined as $\eta \equiv \log_{10}[D(z_{\text{obs}})/D(z_H)]$, which does have a Gaussian distribution. Here, $D(z_{\text{obs}})$ is the comoving distance inferred from the observed redshift (including the peculiar velocity component) and $D(z_H)$ is the true comoving distance, estimated using the Fundamental Plane method (for more detail, see [Springob et al. 2014](#)).

We use a conversion factor to write the model for peculiar velocity in terms of the logarithmic distance ratio:

$$\xi(z_{\text{obs}}) = \frac{1}{\ln(10)} \frac{1 + z_{\text{obs}}}{D(z_{\text{obs}})H(z_{\text{obs}})}. \quad (20)$$

This relation has been previously used for 6dFGS by both Johnson et al. (2014) and Adams & Blake (2017), following work by Hui & Greene (2006) on how peculiar velocities affected supernova magnitudes. For notational simplicity, we do not explicitly state the redshift dependence but note that it is implied by the peculiar velocity that is modified through

$$\eta = \xi v_p. \quad (21)$$

We note that each element of the model covariance corresponds to observations at two points in space, arbitrarily labelled \mathbf{x}_s and \mathbf{x}_t (see fig. 2 of Adams & Blake 2017). Consequently, when discussing how individual covariance elements are modified, we use the notation $C(\mathbf{x}_s, \mathbf{x}_t)$. In the case of the conversion factor ξ , the covariance equations are

$$C_{\eta\eta}(\mathbf{x}_s, \mathbf{x}_t) = \xi^2 C_{vv}(\mathbf{x}_s, \mathbf{x}_t), \quad (22)$$

$$C_{\delta\eta}(\mathbf{x}_s, \mathbf{x}_t) = \xi C_{\delta v}(\mathbf{x}_s, \mathbf{x}_t), \quad (23)$$

$$C_{\eta\delta}(\mathbf{x}_s, \mathbf{x}_t) = \xi C_{v\delta}(\mathbf{x}_s, \mathbf{x}_t). \quad (24)$$

3.3.2 Accounting for Gridding

In this method, gridding allows us to calculate the galaxy overdensity, smooth over non-linear effects, and reduce the computation time required to evaluate the likelihood equation, which scales with the size of the data vector and covariance. We follow the modelling approach outlined by Abate et al. (2008).

Importantly, gridding reduces small-scale power, which we account for by multiplying our model power spectra by a gridding window function Γ , where

$$\Gamma(k, L) = \left\langle \frac{8}{L^3} \frac{\sin\left(k_x \frac{L}{2}\right)}{k_x} \frac{\sin\left(k_y \frac{L}{2}\right)}{k_y} \frac{\sin\left(k_z \frac{L}{2}\right)}{k_z} \right\rangle_{\mathbf{k} \in k}. \quad (25)$$

Here, L is the length of the grid cell in h^{-1} Mpc, and the average is applied to all \mathbf{k} vectors that have magnitude k . Since we may use different gridding sizes for peculiar velocities and overdensities, we define $\Gamma_\delta(k) = \Gamma(k, L_\delta)$ and $\Gamma_v(k) = \Gamma(k, L_v)$.

The smoothing functions are then included in each covariance integrand, such that the covariance components are modified. For example,

$$\mathbf{C}'_{\delta\delta, \beta^0} = \int k^2 P_{mm}(k) \sum_{\ell \in 0, 2, 4} \mathbf{K}_{\delta\delta, \beta^0, \ell} \Gamma_\delta^2(k) dk, \quad (26)$$

$$\mathbf{C}'_{vv, \beta^0} = \int P_{\theta\theta}(k) D_u^2(k, \sigma_u) \sum_{\ell \in 0, 2} \mathbf{K}_{vv, \ell} \Gamma_v^2(k) dk, \quad (27)$$

$$\mathbf{C}'_{v\delta, \beta^0} = \int k P_{\theta m}(k) D_u(k, \sigma_u) \sum_{\ell \in 1, 3} \mathbf{K}_{v\delta, \beta^0, \ell} \Gamma_\delta(k) \Gamma_v(k) dk, \quad (28)$$

and so on for each order of β . The modified covariances may then be summed to give the total smoothed covariances $\mathbf{C}'_{\delta\delta}$, \mathbf{C}'_{vv} and $\mathbf{C}'_{v\delta}$.

In addition to the smoothing, Abate et al. (2008) also correct the velocity auto-covariance after taking the average value in each cell by introducing a shot noise component.

For N_s values of v in a cell at position \mathbf{x}_s , the shot noise contribution can be calculated as

$$\sigma_{\text{sn}}^2(\mathbf{x}_s, \mathbf{x}_t) = \frac{C_{vv}(\mathbf{x}_s, \mathbf{x}_t) - C'_{vv}(\mathbf{x}_s, \mathbf{x}_t)}{N_s} \delta_{st}, \quad (29)$$

where δ_{st} is the Kronecker delta, such that σ_{sn}^2 only appears on the diagonal. This term behaves similarly to an error term, so we incorporate it into the model in the next section.

3.3.3 Inclusion of Error Terms

We incorporate a number of error terms; assuming that the error in any given data point is independent, errors only appear along the diagonal of the covariance matrix.

For the measured value of η at a given position \mathbf{x}_i , we include the uncertainty in the measurement from the Fundamental Plane $\sigma_{\text{obs}}(\mathbf{x}_i)$ (as measured by Springob et al. 2014), the shot noise from averaging the value in each cell σ_{sn} (see Eq. 29), and a stochastic velocity term to account for the breakdown of linear theory σ_v . The contribution to the logarithmic distance ratio auto-covariance will then be

$$\sigma_{\eta\eta}^2(\mathbf{x}_s, \mathbf{x}_t) = \sigma_{\text{obs}}(\mathbf{x}_s) \sigma_{\text{obs}}(\mathbf{x}_t) \delta_{st} + \xi^2 \sigma_{\text{sn}}^2(\mathbf{x}_s, \mathbf{x}_t) + \xi^2 \sigma_v^2 \delta_{st}, \quad (30)$$

where δ_{st} is the Kronecker delta, ensuring that error terms only affect the diagonal of the covariance matrix. The logarithmic distance ratio auto-covariance becomes

$$C_{\eta\eta}^{\text{err}}(\mathbf{x}_s, \mathbf{x}_t) = C'_{\eta\eta}(\mathbf{x}_s, \mathbf{x}_t) + \sigma_{\eta\eta}^2(\mathbf{x}_s, \mathbf{x}_t). \quad (31)$$

For the measured value of δ_g at a given position \mathbf{x}_i , we include the shot noise contribution σ_{δ_g} (discussed in Section 2.1) such that the error contribution to the galaxy overdensity auto-covariance will then be

$$\sigma_{\delta_g \delta_g}^2(\mathbf{x}_s, \mathbf{x}_t) = \sigma_{\delta_g}(\mathbf{x}_s) \sigma_{\delta_g}(\mathbf{x}_t) \delta_{st}. \quad (32)$$

The galaxy overdensity auto-covariance becomes

$$C_{\delta_g \delta_g}^{\text{err}}(\mathbf{x}_s, \mathbf{x}_t) = C'_{\delta_g \delta_g}(\mathbf{x}_s, \mathbf{x}_t) + \sigma_{\delta_g \delta_g}^2(\mathbf{x}_s, \mathbf{x}_t). \quad (33)$$

3.3.4 Accounting for Redshift-Dependent Galaxy Bias

As discussed in Section 2.1, the bias of the galaxy overdensity sample will increase with redshift for our magnitude-limited sample. It is important to account for this effect because the covariance model is a function of the effective bias over the redshift range, rather than the bias as a function of redshift. The amplitude of the cross-correlation is proportional to the linear bias factor, but the value of the bias will be determined by the overdensities that directly influence the peculiar velocities, rather than the entire galaxy overdensity sample. Consequently, we naturally expect that the cross-correlation of peculiar velocities with a lower-bias overdensity sample will not be as strong as that with a higher-bias sample. Given that the peculiar velocity sample is limited to a lower redshift, we anticipate that the effective bias probed by the cross-correlation will be lower than that probed by the galaxy overdensity auto-correlation.

We propose a simple modification that allows for the cross-covariance to have a lower effective bias value than the galaxy overdensity auto-covariance. Until now, the cross-covariance has used the same galaxy bias value as the galaxy

overdensity auto-covariance, b . We modify this using a scaling parameter α_b , such that in the cross-covariance

$$b \rightarrow \alpha_b b, \quad (34)$$

giving the overall transformation

$$C'_{\delta\eta}(\mathbf{x}_s, \mathbf{x}_t) \rightarrow \alpha_b C'_{\delta\eta}(\mathbf{x}_s, \mathbf{x}_t), \quad (35)$$

$$C'_{\eta\delta}(\mathbf{x}_s, \mathbf{x}_t) \rightarrow \alpha_b C'_{\eta\delta}(\mathbf{x}_s, \mathbf{x}_t), \quad (36)$$

while $\mathbf{C}'_{\delta\delta}$ remains unchanged.

3.4 Evaluating the Likelihood

We now cover the key steps required to evaluate our model covariance and the likelihood function.

3.4.1 Generating the Fiducial Power Spectra

To evaluate the covariance model, we must provide model power spectra for our fiducial cosmology. We note that f and b are degenerate with the amplitude of the fiducial power spectra, parametrized by σ_8 . Consequently, our analysis constrains $f\sigma_8$ and $b\sigma_8$ and we divide the power spectra by their fiducial σ_8 value to normalise the amplitude.

We generate the matter power spectrum $P_{mm}(k)$ from the Code for Anisotropies in the Microwave Background (CAMB; Lewis et al. 2000; Lewis & Challinor 2011), utilising the non-linear corrections from Halofit. For the velocity divergence power spectrum $P_{\theta\theta}(k)$ and the cross power spectrum $P_{m\theta}(k) = P_{\theta m}(k)$ we use `velMPTbreeze`, an extension to `MPTbreeze` (Crocce et al. 2012) for calculating velocity power spectra.

We use a number of cosmological parameter sets in our analysis, which are listed in Table 1. When working with the COLA mocks, we use the same cosmological parameters that were used to generate the simulations, which allows us to test whether our method recovers the expected value for $f\sigma_8$. For the 6dFGS data, we use the Planck 2015 cosmological parameter values (Planck Collaboration et al. 2015) for our key results. To test how the choice of cosmological parameters affects our results, we also use cosmological parameters from the Wilkinson Microwave Anisotropy Probe (WMAP) five-year data (Komatsu et al. 2009), and those from the Planck 2018 data (Planck Collaboration et al. 2018).

3.4.2 Integration Bounds

As part of evaluating the covariance equations, we must specify the bounds for the integral over k . We use the same bounds of $k_{\min} = 0.0025 h \text{ Mpc}^{-1}$ and $k_{\max} = 0.15 h \text{ Mpc}^{-1}$ as those from Adams & Blake (2017), but note that we vary k_{\max} during the analysis to understand how it affects our results.

Adams & Blake (2017) found evidence that there was a significant contribution to the galaxy overdensity auto-covariance beyond $k_{\max} = 0.15 h \text{ Mpc}^{-1}$, so introduced an additional integral, that ranged from k_{\max} to $k_{\text{add}} = 1.0 h \text{ Mpc}^{-1}$. We choose to keep this component in the model, and test whether its inclusion is justified when working with the COLA mocks. In doing so, we introduce the bias parameter that scales the additional integral as $b_{\text{add}}\sigma_8$, noting that it behaves similarly to the linear galaxy bias $b\sigma_8$.

Table 1. Cosmological parameters for the four cosmologies used in this analysis. The top section shows the 6 base parameters for standard Λ CDM: physical baryon density; physical dark matter density; reduced Hubble constant; scalar spectral index; scalar amplitude (with pivot point $k_0 = 0.002 h \text{ Mpc}^{-1}$ for the WMAP cosmology and $k_0 = 0.05 h \text{ Mpc}^{-1}$ for the mock and Planck cosmologies); and reionization optical depth. The bottom section shows the fiducial σ_8 for each cosmology, which is a derived parameter.

	COLA Mocks	Planck 2015	WMAP	Planck 2018
$\Omega_b h^2$	0.02210	0.02222	0.02273	0.02212
$\Omega_c h^2$	0.1166	0.1197	0.1099	0.1206
h	0.68	0.6731	0.719	0.6688
n_s	0.96	0.9655	0.963	0.9626
A_s	2.215×10^{-9}	2.195×10^{-9}	2.41×10^{-9}	2.092×10^{-9}
τ	0.09	0.078	0.087	0.0522
σ_8^{fid}	0.82	0.8417	0.7931	0.8118

3.4.3 MCMC Sampling

In this analysis, we constrain our free parameters through a Markov chain Monte Carlo (MCMC) method. We use `emcee` (Foreman-Mackey et al. 2013), which is a `Python` implementation of the affine-invariant ensemble sampler for MCMC proposed by Goodman & Weare (2010). The MCMC chains in our analysis were run with 500 walkers taking 800 steps, which equates to 400,000 samples of our parameter space. We discard the first 150 steps as burn-in and confirm that the chains have converged using the Gelman-Rubin statistic \hat{R} (Gelman & Rubin 1992). If the Gelman-Rubin statistic is close to one, then the chains have converged to the posterior distribution; we use the condition that $\hat{R} - 1$ must be less than 0.05 to satisfy convergence. This convergence test is already implemented as part of the `ChainConsumer` analysis package (Hinton 2016), which we use to analyse all of our `emcee` chains.

The likelihood function (Eq. 1) is evaluated at each step for each walker. The covariance is effectively inverted by applying the Linear Algebra PACKage (LAPACK) Cholesky solver to the equation $\mathbf{C}\mathbf{Y} = \mathbf{\Delta}$, which yields $\mathbf{Y} = \mathbf{C}^{-1}\mathbf{\Delta}$. We use the `Python` implementation of LAPACK available through the `SciPy Linear Algebra` package. The exponent of the likelihood equation is obtained by multiplying \mathbf{Y} by $-\frac{1}{2}\mathbf{\Delta}^T$.

We note that the damping functions for RSD (see Eq. 4 and 6) introduce two parameters (σ_g and σ_u) that cannot be varied as free parameters in the `emcee` runs. This is because they exist inside the integral over the wavenumber k and varying them would involve a recalculation of the entire covariance matrix (which is currently computationally intractable) rather than the simple rescaling that comes from breaking the model covariance into components (see Section 3.2). Consequently, we fix these as part of the analysis but examine how different values affect the results.

4 SIMULATION RESULTS

We wish to validate our method by testing whether our pipeline recovers the expected cosmology used to generate the 6dFGS mock catalogues (see Table 1). For the Ω_m and σ_8

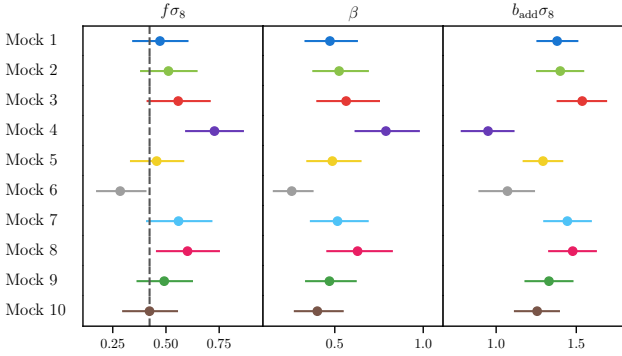


Figure 1. The median values and 68% credible intervals of $f\sigma_8$, β and $b_{\text{add}}\sigma_8$ for ten 6dFGS mocks when using the galaxy overdensity auto-covariance. The expected value for $f\sigma_8$ is shown by the dashed vertical line.

values used to generate the mock catalogues, the expected growth rate of structure is $f\sigma_8 = 0.423$.

The nature of the covariance evaluation means that k_{max} , σ_u and σ_g cannot be varied as free parameters in the analysis. Therefore, it is important to examine whether the choices we make for the values of these parameters affect the constraint on the growth rate. We start by evaluating the likelihood using only the galaxy overdensity and logarithmic distance ratio auto-covariances independently. Once optimal parameter values are established, we fix these and move on to evaluating the likelihood with the complete covariance, testing different values of α_b .

4.1 Galaxy Overdensity Auto-Covariance

We begin by establishing our best estimates for the fixed parameters used in the galaxy overdensity auto-covariance model. The k -range we fit over is controlled by k_{max} , which we take to be $k_{\text{max}} = 0.15 h \text{Mpc}^{-1}$ (see Section 3.4.2). We also include the additional integral, parametrized by the nuisance parameter $b_{\text{add}}\sigma_8$. We do not model RSD in the galaxy overdensity auto-covariance model beyond k_{max} , making the non-linear covariance independent of the growth rate. We set the damping due to pairwise velocities as $\sigma_g = 3.0 h^{-1} \text{Mpc}$; this corresponds to a pairwise velocity dispersion of 300km s^{-1} , which is a standard fiducial assumption (e.g. Peacock & Dodds 1994; Blake et al. 2018). We set the strength of the peculiar velocity power spectrum damping as $\sigma_u = 13.0 h^{-1} \text{Mpc}$, which is the preferred value from Koda et al. (2014). We take the galaxy cross-correlation coefficient to be $r_g = 1$, which corresponds to the linear bias model. We refer to this collection of model parameter values as our fiducial model for the galaxy overdensity auto-covariance.

We start by evaluating the likelihood for the galaxy overdensity measurements from ten 6dFGS mocks using our fiducial model. The marginalised constraints on the three free parameters for this model ($f\sigma_8$, β , $b_{\text{add}}\sigma_8$) are given in Fig. 1. We note that the credible intervals for each parameter have roughly consistent sizes across all ten mocks, which shows that the precision of our method is robust. The fiducial $f\sigma_8$ value is recovered at the 1σ level for seven of the ten mocks. The relative positions of the β credible intervals

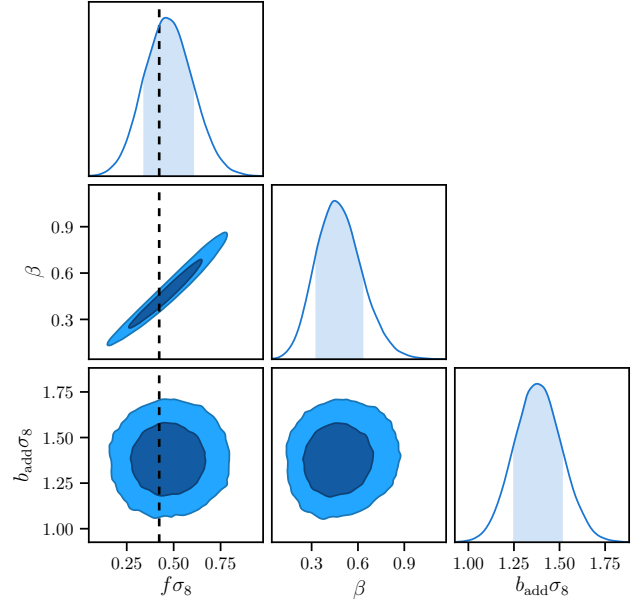


Figure 2. The posteriors of our free parameters for Mock 1 when using the galaxy overdensity auto-covariance. The shaded area of each marginalised posterior represents the 68% credible interval. The dark shading on each contour indicates the 68% credible region and the lighter shading indicates the 95% credible region. The expected value for $f\sigma_8$ is shown by the dashed vertical line.

between each mock are similar to those for $f\sigma_8$, which indicates that the galaxy bias is consistent across the mocks. Given that the mocks are independent, we also calculate the mean and error in the mean for the growth rate, finding $f\sigma_{8,\text{mean}} = 0.51 \pm 0.04$. We note that the mean growth rate is not consistent with the fiducial $f\sigma_8$ value at the 1σ level, likely due to the bias towards higher values visible in Fig. 1. This could be due to the choice of fiducial value for σ_g , which we discuss later in this section.

To get an appreciation for the degeneracies between the three parameters, we show the corner plot for Mock 1, which we take as a representative sample, in Fig. 2. From this, we can see that we recover the expected growth rate of structure at the 1σ level. The contours indicate that there is a slight degeneracy between β and $b_{\text{add}}\sigma_8$, which is to be expected given that Adams & Blake (2017) saw similar behaviour between $b_{\text{fit}}\sigma_8$ and $b_{\text{add}}\sigma_8$ (see fig. 5 in that work). We note that there is minimal degeneracy between $f\sigma_8$ and $b_{\text{add}}\sigma_8$. Finally, the tight slope of the β - $f\sigma_8$ contour indicates that a single effective galaxy bias value is a reasonable model when fitting to linear scales.

Given that several model parameters are fixed, it's important to further investigate how varying these impacts the results, and consequently, whether our choice of parameters for the fiducial model is justified. Before proceeding, we note that the maximum likelihood for our fiducial model corresponds to $\chi^2 = 1581.88$ ($\chi^2/\text{dof} = 0.97$), indicating a reasonable fit.

Firstly, we assess whether we are justified in using $b_{\text{add}}\sigma_8$ as a nuisance parameter. We run the covariance model while excluding $b_{\text{add}}\sigma_8$ and present the median values and 68% credible intervals for $f\sigma_8$ and β relative to those from the fiducial model in Fig. 3. The maximum like-

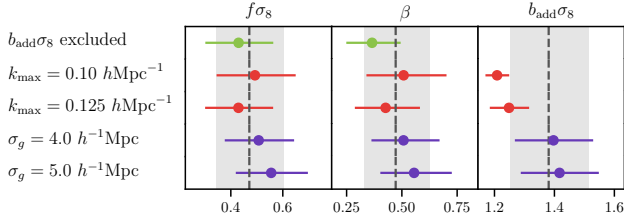


Figure 3. The median values and 68% credible intervals of $f\sigma_8$, β and $b_{\text{add}}\sigma_8$ for various tests on Mock 1 when using the galaxy overdensity auto-covariance. The dashed lines and grey shaded regions represent the median value and 68% credible interval for our fiducial model: $b_{\text{add}}\sigma_8$ included, $k_{\text{max}} = 0.15 h \text{ Mpc}^{-1}$, $\sigma_g = 3.0 h^{-1} \text{ Mpc}$.

likelihood when excluding $b_{\text{add}}\sigma_8$ from the model corresponds to $\chi^2 = 1680.45$ ($\chi^2/\text{dof} = 1.03$). We can see that excluding $b_{\text{add}}\sigma_8$ lowers both $f\sigma_8$ and β . The effect on β is greater because the additional power that was being contributed from the non-zero $b_{\text{add}}\sigma_8$ has been transferred to the linear-scale bias, lowering β for a fixed growth rate. We determine that the difference in χ^2 between including and excluding $b_{\text{add}}\sigma_8$, interpreted using the reduced Akaike information criterion (AICc; see [Burnham & Anderson 2004](#)), is substantial evidence for keeping $b_{\text{add}}\sigma_8$ as a model parameter.

Next, we test how the value of k_{max} affects the constraints. We run the covariance model while setting $k_{\text{max}} = 0.10, 0.125 h \text{ Mpc}^{-1}$ and present the median values and 68% credible intervals for $f\sigma_8$, β and $b_{\text{add}}\sigma_8$ relative to those from the fiducial model in Fig. 3. The maximum likelihood when setting $k_{\text{max}} = 0.10 h \text{ Mpc}^{-1}$ corresponds to $\chi^2 = 1578.90$ ($\chi^2/\text{dof} = 0.97$). The maximum likelihood when setting $k_{\text{max}} = 0.125 h \text{ Mpc}^{-1}$ corresponds to $\chi^2 = 1581.35$ ($\chi^2/\text{dof} = 0.97$). Given the minimal impact of this choice on the measured growth rate and likelihood, we choose to keep our fiducial model value of $k_{\text{max}} = 0.15 h \text{ Mpc}^{-1}$ as it maximises the range over which $f\sigma_8$ is fit.

Finally, we also test how the value of σ_g affects the constraints. We run the covariance model while setting $\sigma_g = 4.0, 5.0 h^{-1} \text{ Mpc}$ and present the median values and 68% credible intervals for $f\sigma_8$, β and $b_{\text{add}}\sigma_8$ relative to those from the fiducial model in Fig. 3. The maximum likelihood when setting $\sigma_g = 4.0 h^{-1} \text{ Mpc}$ corresponds to $\chi^2 = 1580.22$ ($\chi^2/\text{dof} = 0.97$). The maximum likelihood when setting $\sigma_g = 5.0 h^{-1} \text{ Mpc}$ corresponds to $\chi^2 = 1579.86$ ($\chi^2/\text{dof} = 0.97$). We can see that there is a systematic shift in both $f\sigma_8$ and β in proportion to the value of σ_g , while $b_{\text{add}}\sigma_8$ remains largely unaffected. This is consistent with the fact that σ_g controls the level of damping and that stronger damping will result in larger $f\sigma_8$ values as the covariance compensates, similar to the trade-off between β and $b_{\text{add}}\sigma_8$. This effect has also been seen in other RSD studies (see figure 4 in [Peacock et al. 2001](#)). We also attempted to run tests using $\sigma_g = 2.0, 1.0 h^{-1} \text{ Mpc}$. Unfortunately, the numerical integration library we used to calculate the covariance matrix elements failed in both cases due to round-off errors. Given the trend of $f\sigma_8$ with σ_g , we keep $\sigma_g = 3.0 h^{-1} \text{ Mpc}$ as our fiducial value.

Out of all three tests, Fig. 3 shows us that σ_g has the largest effect on $f\sigma_8$ and that the value of k_{max} has the largest effect on $b_{\text{add}}\sigma_8$. For $f\sigma_8$, the various systematic tests

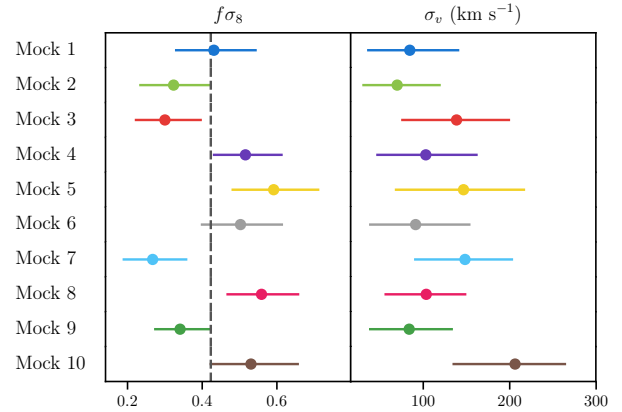


Figure 4. The median values and 68% credible intervals of $f\sigma_8$ and σ_v for ten 6dFGS mocks when using the logarithmic distance ratio auto-covariance. The expected value for $f\sigma_8$ is shown by the dashed vertical line.

all return median values that are within 1σ of our fiducial case. We later use these tests to quantify the systematic uncertainty for our parameter estimates when working with the 6dFGS data in Section 5.1.

4.2 Logarithmic Distance Ratio Auto-Covariance

Again, we begin by establishing our best estimates for the fixed parameters used in the logarithmic distance ratio auto-covariance model. We again take $k_{\text{max}} = 0.15 h \text{ Mpc}^{-1}$ as the boundary to our fitted k -range. The damping identified by [Koda et al. \(2014\)](#) is implemented as a sinc function and parametrized by σ_u (see Eq. 6). We take $\sigma_u = 13.0 h^{-1} \text{ Mpc}$ as our best estimate, given that [Koda et al. \(2014\)](#) found this to be the best fit to their simulations. We refer to this collection of model parameter values as our fiducial model for the logarithmic distance ratio auto-covariance.

As in the previous section, we examine the constraints for all ten mocks when using our best estimates. The marginalised constraints for the free parameters of this model ($f\sigma_8$, σ_v) are given in Fig. 4. As with the galaxy overdensity auto-covariance, the credible intervals for our free parameters are roughly consistent across all ten mocks. The method does not appear to be biased; the ten mocks are evenly distributed around the expected recovery value for $f\sigma_8$, and the value is recovered at the 1σ level in six of the ten mocks. Given that the mocks are independent, we also calculate the mean and error in the mean for the growth rate, finding $f\sigma_{8,\text{mean}} = 0.44 \pm 0.03$. We note that the mean growth rate is consistent with the fiducial $f\sigma_8$ value at the 1σ level.

We again take Mock 1 as a representative sample and present the corner plot for this mock in Fig. 5. There appears to be minimal degeneracy between $f\sigma_8$ and σ_v , and the expected growth rate is well-recovered by the mock. The maximum likelihood for our fiducial model corresponds to $\chi^2 = 1054.78$ ($\chi^2/\text{dof} = 0.91$), indicating a reasonable fit.

As in the previous section, we test how varying our fixed parameters alters the results, beginning with k_{max} . We run the covariance model while setting $k_{\text{max}} = 0.10, 0.125 h \text{ Mpc}^{-1}$ and present the median values and 68% cred-

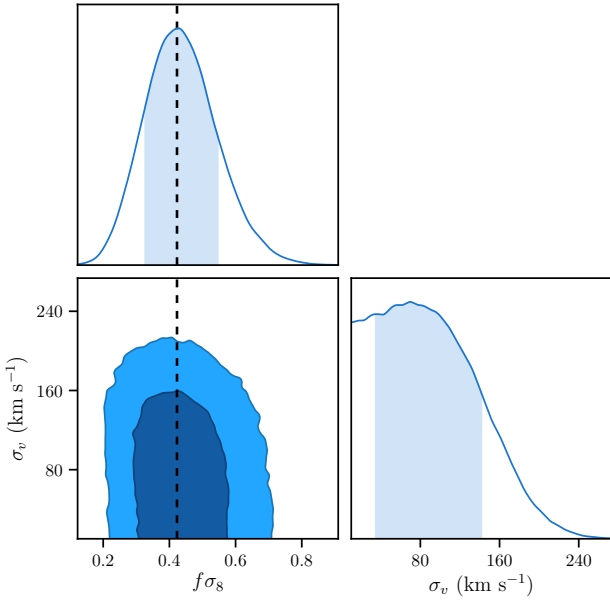


Figure 5. The posteriors of our free parameters for Mock 1 when using the logarithmic distance ratio auto-covariance. The shaded area of each marginalised posterior represents the 68% credible interval. The dark shading on each contour indicates the 68% credible region and the lighter shading indicates the 95% credible region. The expected value for $f\sigma_8$ is shown by the dashed vertical line.

ible intervals for $f\sigma_8$ and σ_v relative to those from the fiducial model in Fig. 6. The maximum likelihood when setting $k_{\max} = 0.10 \, h \, \text{Mpc}^{-1}$ corresponds to $\chi^2 = 1055.09$ ($\chi^2/\text{dof} = 0.91$). The maximum likelihood when setting $k_{\max} = 0.125 \, h \, \text{Mpc}^{-1}$ corresponds to $\chi^2 = 1055.00$ ($\chi^2/\text{dof} = 0.91$). We can see that changing the value of k_{\max} has a negligible effect on the constraints from the logarithmic distance ratio auto-covariance. This is supported by the χ^2 values, which only vary on the order of 0.1 between the three runs. Consequently, we choose to keep our best estimate of $k_{\max} = 0.15 \, h \, \text{Mpc}^{-1}$ as our value for the fiducial model.

We also test how changing the value of the damping parameter σ_u affects constraints. We run the covariance model while setting $\sigma_u = 11.0, 15.0, 17.0 \, h^{-1} \, \text{Mpc}$ and present the median values and 68% credible intervals for $f\sigma_8$ and σ_v relative to those from the fiducial model in Fig. 6. Again, the difference between our tested values is negligible, although we do see a slight trend in $f\sigma_8$, where lower values of σ_u correspond to lower growth rates. This is consistent with the behaviour of the damping function, where lowering σ_u results in less damping and a higher growth rate. Similarly to the k_{\max} test, the χ^2 values only vary on the order of 0.1. Given that our best estimate of σ_u provides a good fit, we choose to keep this as the value for our fiducial model.

Out of the two fixed model parameters, Fig. 3 shows us that σ_u has the largest effect on $f\sigma_8$, but it is still minimal. σ_v is unaffected by both the values of k_{\max} and σ_u . For $f\sigma_8$, the various tests all return median values that are well within 1σ of our fiducial case. We later use these tests to quantify the systematic uncertainty for our parameter estimates when working with the 6dFGS data in Section 5.1.

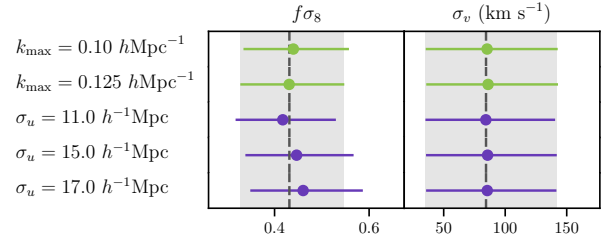


Figure 6. The median values and 68% credible intervals of $f\sigma_8$ and σ_v for various tests on Mock 1 when using the logarithmic distance ratio auto-covariance. The dashed lines and grey shaded regions represent the median value and 68% credible interval for our fiducial model: $k_{\max} = 0.15 \, h \, \text{Mpc}^{-1}$, $\sigma_u = 13.0 \, h^{-1} \, \text{Mpc}$.

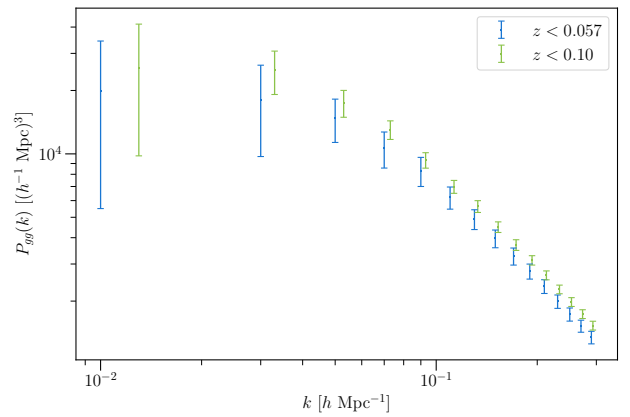


Figure 7. The mean and standard deviation of the galaxy-galaxy power spectrum from 600 mock catalogues, with uncertainties corresponding to those for one mock. The amplitude of the power spectrum for the $z < 0.057$ sample is clearly lower than that for the $z < 0.10$ sample, indicating that the lower redshift sample has a lower effective bias. We note that the $z < 0.10$ points have been shifted to the right by $\Delta k = 0.003 \, h \, \text{Mpc}^{-1}$ for clarity.

4.3 Complete Covariance

When running the full covariance model, we use the fiducial set-up that we established in the previous two sections: $b_{\text{add}}\sigma_8$ included as a free parameter, $k_{\max} = 0.15 \, h \, \text{Mpc}^{-1}$ for both auto-covariances and the cross-covariance, $\sigma_g = 3.0 \, h^{-1} \, \text{Mpc}$ for the galaxy overdensity auto-covariance and cross-covariance, and $\sigma_u = 13.0 \, h^{-1} \, \text{Mpc}$ for the logarithmic distance ratio auto-covariance and cross-covariance. In addition to these, we have also introduced a new parameter for the cross-covariance, α_b , which modifies the effective galaxy bias for the cross-covariance relative to that of the galaxy overdensity auto-covariance.

Before proceeding, we establish that the effective bias of our sample is different for different redshift ranges. We do this by estimating the galaxy-galaxy power spectrum for two redshift ranges, using the 600 mock catalogues developed by Carter et al. (2018) and discussed in Section 2.2. The redshift ranges correspond to the limits of our logarithmic distance ratio sample ($z < 0.057$) and our galaxy overdensity sample ($z < 0.1$). We show the two estimated power spectra in Fig. 7.

Nominally, we could estimate α_b^2 directly by taking the

ratio of the two estimated power spectra (recalling that the amplitude of the galaxy power spectrum is proportional to b^2). The ratio between each pair of points implies $\alpha_b = 0.94 \pm 0.03$, where the uncertainty is scaled to a single mock. However, we still choose to run the model for different values of α_b before selecting the fiducial value. We do this for two key reasons. Firstly, it is not trivial to estimate the redshift range that the logarithmic distance ratio sample (and hence the cross-covariance) is sensitive to. Adams & Blake (2017) showed that the cross-correlation is non-zero up to separations of at least $50 h^{-1}$ Mpc, depending on the orientation of the galaxy overdensity-logarithmic distance ratio pair (see fig. 9 and surrounding text in that work). This means that the effective bias for the cross-correlation is likely affected by overdensities beyond the boundary of the logarithmic distance ratio sample, a subtlety that the estimated value of α_b from the power spectra ratio does not account for. Secondly, α_b may be sensitive to additional effects beyond the difference in effective bias. For example, Eq. 35 and 36 show that α_b reduces the amplitude of the cross-covariance relative to the two auto-covariances (although we note that α_b only reduces the amplitude of the β^0 term and does not affect the β^1 term, see Eq. 17). Additionally, it's possible that the relative weight of different regions towards the signal-to-noise differs between the cross-covariance and the galaxy overdensity auto-covariance. Given these two factors, we determine that it is more appropriate to estimate the value of α_b by requiring recovery of the expected $f\sigma_8$ value when working with the mocks.

We start by running the full covariance model on our representative mock (Mock 1) with different values of α_b . The lowest value we test is $\alpha_b = 0.70$; we consider lower values to be unphysical as they would translate to differences in the effective galaxy bias values that are implausible. The posteriors are shown in Fig. 8.

Fig. 8 indicates that for the representative mock, the growth rate is recovered at the 1σ level for all values of α_b aside from $\alpha_b = 0.95$. There is a clear systematic trend (although it is by no means linear) in that larger values of α_b correspond to lower values of $f\sigma_8$. Additionally, we see that the posterior for $f\sigma_8$ widens as α_b becomes lower and that the posteriors appear to be converging. This behaviour ties back to the fact that α_b reduces the amplitude of the cross-covariance model, causing it to contribute less to the overall covariance. The increase in the value of $f\sigma_8$ and the widening of the posterior is consistent with the model favouring the auto-covariance information above the cross-covariance information. We note that the constraints from the low- α_b cases are still better than the galaxy overdensity auto-covariance only case, since the logarithmic distance ratio auto-covariance is also contributing to the constraints. This interpretation also explains the behaviour of σ_v , which tends towards the logarithmic distance ratio auto-covariance constraint as α_b is lowered (see Fig. 5 for comparison). It's clear that the cross-covariance has little influence on $b_{\text{add}}\sigma_8$, and consequently, the constraints are very close to those from the galaxy overdensity auto-covariance (see Fig. 2).

Given the systematic behaviour with α_b , we choose to fix its value at $\alpha_b = 0.90$. This maximises the amount of cross-covariance information used, while still recovering the growth rate of structure at the 1σ level. The maximum likelihood for this fit corresponds to $\chi^2 = 2615.90$ ($\chi^2/\text{dof} =$

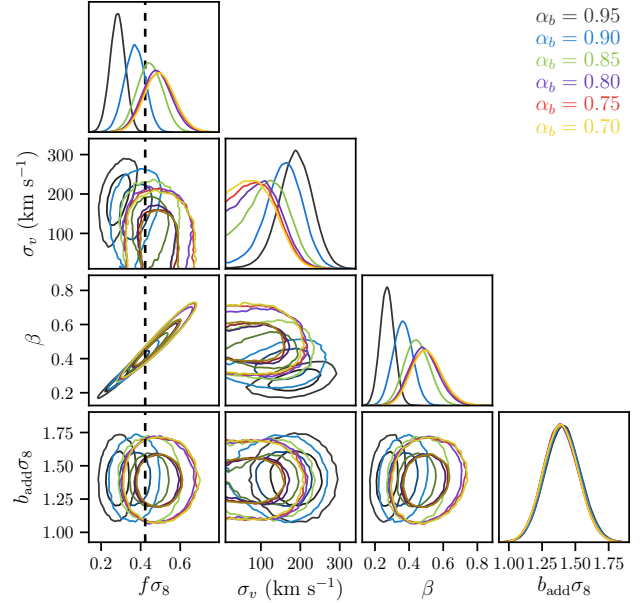


Figure 8. The posteriors of $f\sigma_8$, σ_v , β and $b_{\text{add}}\sigma_8$ for the complete covariance model fit to Mock 1 for different values of α_b . The inner contour indicates the 68% credible region and the outer contour indicates the 95% credible region. The expected value for $f\sigma_8$ is shown by the dashed vertical line.

Table 2. Median values (with 68% credible intervals) of $f\sigma_8$, σ_v , β and $b_{\text{add}}\sigma_8$ for the galaxy overdensity auto-covariance, logarithmic distance ratio auto-covariance and complete covariance models for Mock 1.

Model	$f\sigma_8$	σ_v (km s $^{-1}$)	β	$b_{\text{add}}\sigma_8$
$\mathbf{C}_{\delta_g\delta_g, \text{RSD}}^{\text{err}}$	0.47 ± 0.13	—	$0.47^{+0.16}_{-0.14}$	1.38 ± 0.13
$\mathbf{C}_{\eta\eta, \text{RSD}}^{\text{err}}$	$0.43^{+0.11}_{-0.10}$	84^{+57}_{-49}	—	—
\mathbf{C}	$0.370^{+0.053}_{-0.052}$	159^{+45}_{-50}	0.363 ± 0.058	1.40 ± 0.13

0.94), which is reasonable. We note that we account for the systematic behaviour from α_b by calculating a systematic error for our final 6dFGS growth rate constraint in Section 5.1.

Finally, we show the median values and 68% credible intervals for our free parameters when running the complete covariance model with $\alpha_b = 0.90$ on all ten mocks in Fig. 9. The recovery of $f\sigma_8$ is reasonable across all ten mocks, validating our choice of $\alpha_b = 0.90$ as the fiducial value for the remainder of the analysis. Given that the mocks are independent, we also calculate the mean and error in the mean for the growth rate, finding $f\sigma_{8, \text{mean}} = 0.40 \pm 0.02$. We note that the mean growth rate is consistent with the fiducial $f\sigma_8$ value at the 1σ level.

4.4 Summary of Fiducial Model Results

We summarise the key constraints from running our fiducial model on our representative mock for the three covariance model cases in Table 2. It is clear that the uncertainty in the growth rate of structure has reduced significantly when using the complete covariance in comparison to using either

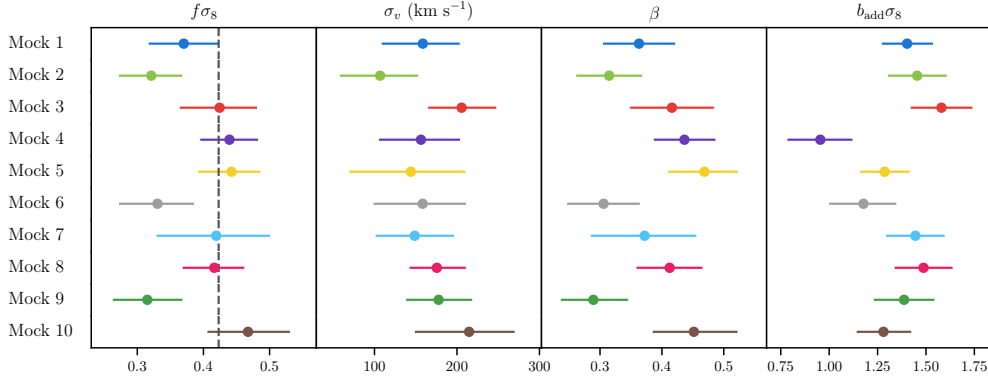


Figure 9. The median values and 68% credible intervals of $f\sigma_8$, σ_v , β and $b_{\text{add}}\sigma_8$ for ten 6dFGS mocks when using the complete covariance with $\alpha_b = 0.90$. The expected value for $f\sigma_8$ is shown by the dashed vertical line.

of the auto-covariances alone: we see a 60% improvement in the uncertainty from the galaxy overdensity auto-covariance and a 50% improvement in the uncertainty from logarithmic distance ratio auto-covariance. For β the uncertainty improvement is 61% when going from the galaxy overdensity auto-covariance to the complete covariance. Given the sophistication of the mocks, we expect to see similar improvements when applying our fiducial model to the data in the next section.

While we believe that the reduction in uncertainty can be entirely attributed to the introduction of the cross-covariance, we note that tighter uncertainties can be a symptom of underlying tension in the model or data sets. Given the consistency of the growth rate constraints and that the complete covariance model shows a reasonable χ^2/dof (0.94), we do not believe that tension is impacting the uncertainty reduction.

5 DATA RESULTS

After comprehensive testing on the 6dFGS mock catalogues, we run the galaxy overdensity auto-covariance, logarithmic distance auto-covariance and complete covariance models on the 6dFGS dataset. The models use the fiducial parameter values from the previous section: $k_{\text{max}} = 0.15 h \text{ Mpc}^{-1}$, $\sigma_g = 3.0 h^{-1} \text{ Mpc}$, $\sigma_u = 13.0 h^{-1} \text{ Mpc}$, $r_g = 1.0$, and $\alpha_b = 0.90$. Now that we are working with real data, we choose the fiducial cosmology to be that from [Planck Collaboration et al. \(2015\)](#), which is summarised in Table 1. Given that we are working with a complete RSD model for our overdensity data, we directly compare our results to those from [Beutler et al. \(2012\)](#), who found $f\sigma_8 = 0.423 \pm 0.055$ and $\beta = 0.373 \pm 0.054$ at an effective redshift of $z_{\text{eff}} = 0.067$. These are the most precise measurements of $f\sigma_8$ and β available for 6dFGS, so serve as a useful point of comparison. We present the posteriors of our free parameters in Fig. 10, the corresponding median constraints (with 68% confidence intervals) in Table 3 and maximum likelihood values (with the corresponding χ^2 values) in Table 4. For the galaxy overdensity auto-covariance we find $f\sigma_8 = 0.41^{+0.15}_{-0.14}$, for the logarithmic distance ratio auto-covariance we find $f\sigma_8 = 0.53^{+0.11}_{-0.10}$, and for the complete covariance we find $f\sigma_8 = 0.384 \pm 0.052$.

We find that our measurements of $f\sigma_8$ and β for the

Table 3. Median values (with 68% credible intervals) of $f\sigma_8$, σ_v , β and $b_{\text{add}}\sigma_8$ for 6dFGS using the galaxy overdensity auto-covariance ($\mathbf{C}_{\delta\delta}$), the logarithmic distance ratio auto-covariance ($\mathbf{C}_{\eta\eta}$), and the complete covariance (\mathbf{C}).

Model	$f\sigma_8$	$\sigma_v \text{ (km s}^{-1}\text{)}$	β	$b_{\text{add}}\sigma_8$
$\mathbf{C}_{\delta\delta}$	$0.41^{+0.15}_{-0.14}$	—	$0.30^{+0.13}_{-0.11}$	$1.45^{+0.17}_{-0.16}$
$\mathbf{C}_{\eta\eta}$	$0.53^{+0.11}_{-0.10}$	90^{+54}_{-50}	—	—
\mathbf{C}	0.384 ± 0.052	208^{+44}_{-45}	$0.289^{+0.044}_{-0.043}$	1.53 ± 0.17

Table 4. Maximum likelihood values of $f\sigma_8$, σ_v , β and $b_{\text{add}}\sigma_8$ for 6dFGS using the galaxy overdensity auto-covariance ($\mathbf{C}_{\delta\delta}$), the logarithmic distance ratio auto-covariance ($\mathbf{C}_{\eta\eta}$), and the complete covariance (\mathbf{C}). We also include the χ^2 and χ^2/dof statistic for the maximum likelihood values

Model	$f\sigma_8$	$\sigma_v \text{ (km s}^{-1}\text{)}$	β	$b_{\text{add}}\sigma_8$	χ^2	χ^2/dof
$\mathbf{C}_{\delta\delta}$	0.38	—	0.27	1.45	1774.45	1.09
$\mathbf{C}_{\eta\eta}$	0.52	84	—	—	847.69	0.94
\mathbf{C}	0.380	208	0.286	1.52	2610.42	1.03

three covariance analyses are self-consistent. We have hence demonstrated that peculiar velocities and redshift-space distortions provide consistent measurements of the growth rate of structure for the same galaxy survey and modelling framework. Given that the two probes constrain the growth rate on different physical scales (peculiar velocities are sensitive to larger scales than RSD), the complete covariance analysis may be a promising way to test modified gravity models, which is a promising avenue for future work. We also note that our value of $f\sigma_8$ is consistent at close to the 1σ level with the Planck 2015 + GR prediction of $f\sigma_8 = 0.446$ at redshift $z = 0$ and at the 1σ level with the Planck 2018 + GR prediction of $f\sigma_8 = 0.430$ at redshift $z = 0$.

We calculate that the percentage uncertainties in $f\sigma_8$ are 35% for the galaxy overdensity auto-covariance, 20% for the logarithmic distance ratio auto-covariance and 14% for the complete covariance. Most importantly, we see a 64% reduction in the uncertainty when going from the galaxy overdensity auto-covariance to the complete covariance, and a 50% reduction when going from the logarithmic distance ratio auto-covariance to the complete covariance.

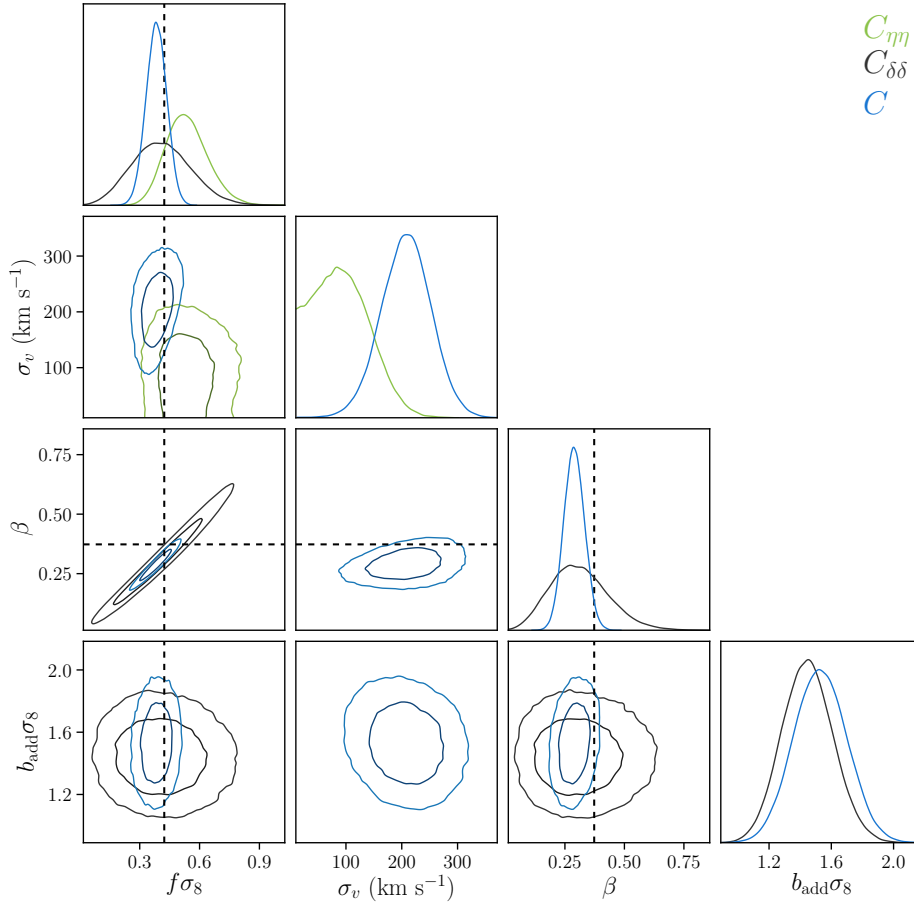


Figure 10. The posteriors of $f\sigma_8$, β , $b_{\text{add}}\sigma_8$ and σ_v for 6dFGS when using the galaxy overdensity auto-covariance ($\mathbf{C}_{\delta\delta}$), the logarithmic distance ratio auto-covariance ($\mathbf{C}_{\eta\eta}$), and the complete covariance (\mathbf{C}). The results for $f\sigma_8$ and β from [Beutler et al. \(2012\)](#) are indicated by the dashed lines.

The improvement in going from the galaxy overdensity auto-covariance to the complete covariance is most notable in the $f\sigma_8$ - β contour of Fig. 10, where the 2σ contour from the complete covariance sits well inside the 1σ contour from the auto-covariance.

It’s also worth highlighting that the consistent $f\sigma_8$ - β slope between the galaxy overdensity auto-covariance and the complete covariance indicates that the two models prefer similar effective galaxy bias values. We note that this would not be the case without an appropriate value for α_b , which allows the cross-covariance to be parametrized in terms of the galaxy overdensity sample’s effective bias.

5.1 Systematics

Given the increased precision of our constraint on the growth rate of structure, it is important to investigate how robust our result is to various systematics. This includes the fixed parameters of our covariance model (k_{max} , σ_g , σ_u and α_b), as well as the underlying cosmological parameters which inform the power spectrum models. Note that we do not investigate the systematic effects of changing r_g , as we chose to leave this as a fixed parameter corresponding to the assumption of the linear bias model (see Section 4.1). Future work could

potentially vary this parameter, although we note it is highly degenerate with the growth rate of structure.

5.1.1 Sensitivity to Fixed Parameters

For the fixed parameters, we’re able to estimate a systematic error contribution by varying the values of the fixed parameters and re-running the model. We assume that each systematic is independent, allowing us to vary a single parameter while holding the others fixed at their fiducial values. For each systematic $s \in (k_{\text{max}}, \sigma_g, \sigma_u, \alpha_b)$, the systematic variance in parameter ϕ is

$$\sigma_s^2 = \left(\frac{\partial \phi}{\partial s} \right)^2 (\Delta s)^2, \quad (37)$$

where we approximate the partial derivative using the central finite difference method:

$$\frac{\partial \phi}{\partial s} \approx \frac{\phi(s + \Delta s) - \phi(s - \Delta s)}{2\Delta s}. \quad (38)$$

We note that σ_s^2 are the diagonal elements of the full systematic covariance (e.g. eq. C4 in [Zhang et al. 2017](#)). We then give the total systematic error as the sum in quadrature of

Table 5. The systematic standard deviation contributions to $f\sigma_8$ and β for each fixed parameter.

Parameter	$\sigma_{k_{\max}}$	σ_{σ_g}	σ_{σ_u}	σ_{α_b}
$f\sigma_8$	1.69×10^{-3}	2.84×10^{-3}	1.09×10^{-3}	6.06×10^{-2}
β	3.30×10^{-3}	8.97×10^{-4}	1.08×10^{-3}	4.84×10^{-2}

each systematic:

$$\sigma_{\text{sys}} = \sqrt{\sum_{i=s} \sigma_i^2}. \quad (39)$$

We note that the size of the systematic variance will be affected by the step size Δs . Consequently, we mostly use the same step sizes that we used when testing each fixed parameter throughout the simulation analysis in Section 4, which were chosen to encompass reasonable values for the fixed parameters. The only exception is in the case of α_b , where we choose a smaller step size of $\Delta\alpha_b = 0.025$, as the step size of $\Delta\alpha_b = 0.05$ gives posteriors that recover the growth rate outside the 1σ level (see Fig. 8). The systematic standard deviation values are given in Table 5 for $f\sigma_8$ and β , noting that we don't provide systematic standard deviation estimates for our two nuisance parameters σ_v and $b_{\text{add}}\sigma_8$ since they are already marginalised over in the model fits. It's clear that α_b is the dominant systematic for both $f\sigma_8$ and β , with a systematic standard deviation that is at least an order of magnitude larger than any of the other fixed parameters.

From this analysis, our final constraint (using the full covariance model) is $f\sigma_8 = 0.384 \pm 0.052(\text{stat}) \pm 0.061(\text{sys})$ for the growth rate of structure, and $\beta = 0.289^{+0.044}_{-0.043}(\text{stat}) \pm 0.049(\text{sys})$ for the redshift-space distortion parameter. Currently, the systematic error for each parameter is greater than the corresponding statistical uncertainty, which is driven by the behaviour of α_b , specifically, its large degeneracy with $f\sigma_8$. Given that our introduction of α_b is a relatively simple method for accounting for the difference in effective bias across our samples, we believe that this systematic could be reduced or mitigated in future work, and suggest some avenues for this in Section 5.3.

5.1.2 Sensitivity to Cosmological Parameters

Our method is affected by the cosmological parameter values (those listed in Table 1) in two key ways. Firstly, through the transformation of the observed coordinates (RA, dec, z) to Cartesian coordinates (x , y , z) in configuration space, which is required for our covariance model. Secondly, the cosmological parameters influence the shape of all three model power spectra P_{mm} , $P_{\theta\theta}$ and $P_{m\theta}$. We note that the second point is more important, since the transformations from observed to Cartesian coordinates are independent of all the cosmological parameters to first order, being at low redshift and with distances measured in h^{-1} Mpc units.

To test how sensitive our $f\sigma_8$ constraint is to the choice of the cosmological parameter values, we use the values from the three CMB analyses listed in Table 1: the WMAP Year-5 results (Komatsu et al. 2009), Planck 2015 results (our fiducial model; Planck Collaboration et al. 2015) and the Planck 2018 results (Planck Collaboration et al. 2018). We repeat

our analysis for the complete covariance, including the data transformation, for the two additional cosmological parameter sets, and present the median values and 68% credible intervals for $f\sigma_8$, σ_v , β and $b_{\text{add}}\sigma_8$ for all three parameter sets in Fig. 11. It's clear from the figure that the choice of cosmological parameters has little effect on $f\sigma_8$.

5.2 Comparison to Existing Literature

5.2.1 Covariance Analysis

Using a combined auto- and cross- covariance model without redshift-space distortions (RSD), Adams & Blake (2017) found $f\sigma_8 = 0.424^{+0.065}_{-0.062}$ and $\beta = 0.300^{+0.048}_{-0.046}$, which we compare to the constraints from this analysis of $f\sigma_8 = 0.384 \pm 0.052(\text{stat}) \pm 0.061(\text{sys})$ and $\beta = 0.289^{+0.044}_{-0.043}(\text{stat}) \pm 0.049(\text{sys})$. For $f\sigma_8$, the statistical uncertainty is reduced by 18% and our result is consistent at the 1σ level. For β , the statistical uncertainty is reduced by 7.4% and our result is consistent at the 1σ level. We believe that the improvement in the statistical uncertainty comes from two sources: the improved covariance model, which now utilises the growth rate information present in RSD, and the larger galaxy overdensity sample used in this analysis. The improvement from the larger sample is due to two factors: there are more covariance entries because we've extended to higher redshift ($N_{\delta_g} = 1633$ cells compared to $N_{\delta_g} = 1036$ cells) and a larger number of galaxies per cell at low redshift (which comes from no longer having the volume-limited sample), reducing the shot noise. We suspect that the overall improvement in the statistical uncertainty may also be slightly limited by the fact that we used a larger gridding scale, smoothing over more of the small-scale information. We show a visual comparison of the covariance constraints in Fig. 12.

5.2.2 Multi-Tracer Approaches

In this study, we have demonstrated the benefits of using the shared information from multiple tracers, which supports the results of theoretical studies (e.g. McDonald & Seljak 2009; Gil-Marín et al. 2010; Bernstein & Cai 2011; Abramo & Leonard 2013). We compare the improvements we see in the statistical uncertainty to those seen by Blake et al. (2013), who presented the first multi-tracer approach applied to galaxy overdensity data from the Galaxy And Mass Assembly (GAMA) survey. In that study, they used two different galaxy overdensity samples with different galaxy bias values, comparing the power spectra of these samples to models, including the cross-power spectrum. Depending on the sample, they found a 10-20% improvement in their constraints of the growth rate when utilising the cross-power spectrum. In our analysis, we see significantly better improvements: 50% improvement compared to the logarithmic distance ratio only sample, and 64% improvement compared to the galaxy overdensity only sample. We believe that this is due, in part, to the strong independent constraints that the logarithmic distance ratio places on the growth rate. When coupled with the fact that the two samples (and their cross-correlation) constrain the growth rate in different ways, we believe that this explains our larger improvement on the growth rate constraint compared to the analysis from Blake et al. (2013), which only utilised RSD information.

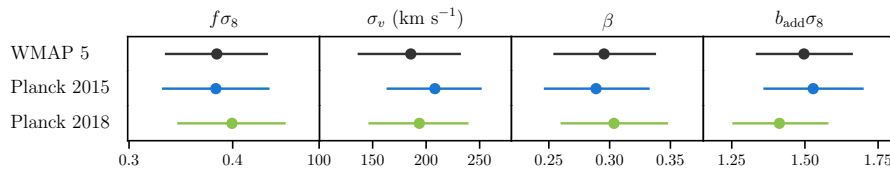


Figure 11. The median values and 68% credible intervals of $f\sigma_8$, σ_v , β and $b_{\text{add}}\sigma_8$ for 6dFGS when using three sets of cosmological parameters, as listed in Table 1.

5.2.3 Forecasts for the 6dFGS Cross-Covariance Analysis

We also compare our relative constraints to those forecast for 6dFGS from two studies that use the Fisher matrix formalism: [Koda et al. \(2014\)](#) and [Howlett et al. \(2016\)](#). Both studies use the same RSD model as we do and forecast the relative constraints that can be obtained on $f\sigma_8$ for various samples of 6dFGS.

[Koda et al. \(2014\)](#) use 6dFGSv as the basis for both their galaxy overdensity and logarithmic distance ratio sample, and model the various covariances out to $k_{\text{max}} = 0.1 h \text{ Mpc}^{-1}$. They forecast a 25% constraint on $f\sigma_8$ for the logarithmic distance ratio auto-covariance and 15% when using the complete covariance. For β , they forecast a 16% constraint when using the complete covariance. We find a relative constraint on $f\sigma_8$ of 20% for the logarithmic distance ratio auto-covariance and 14% for the complete covariance, and a relative constraint on β of 15% for the complete covariance. In this analysis, we find a constraint from the logarithmic distance ratio auto-covariance that is better than forecast, and note that this was also the case in [Adams & Blake \(2017\)](#) and [Johnson et al. \(2014\)](#). This could be due to differences between the assumptions that went into the forecasting and our own analysis. We should expect to do better than [Koda et al. \(2014\)](#) because our galaxy overdensity sample goes to a higher redshift ($z = 0.1$ compared to $z = 0.057$), which we find to be the case, but only by a single percentage point.

[Howlett et al. \(2016\)](#) used the complete 6dFGSv sample as the basis for their logarithmic distance ratio sample and close to the complete 6dFGSz sample as the basis for their galaxy overdensity sample (the upper limit on the redshift for their sample is $z = 0.2$). Like [Koda et al. \(2014\)](#), they model the various covariances out to $k_{\text{max}} = 0.1 h \text{ Mpc}^{-1}$. They forecast a 25.1% constraint on $f\sigma_8$ for the logarithmic distance ratio auto-covariance and 11.2% when using the complete covariance. For β , they forecast a 12.3% constraint when using the complete covariance. The similarity of their logarithmic distance ratio auto-covariance constraint to that from [Koda et al. \(2014\)](#) is consistent with the fact that they used very similar samples. The forecast constraints are better than our statistical uncertainties, which is unsurprising given they used a larger galaxy overdensity sample.

As a final point, we note that both of these analyses assume that the galaxy overdensity auto-correlation and cross-correlation are responding to the same effective bias. At this stage, it is unclear what effect this might have on the precision of forecasting, since we found that the value of the relative effective bias (parametrized by α_b in our study) has a significant effect on the posterior of $f\sigma_8$.

5.2.4 6dFGS Redshift-Space Distortion and Velocity Results

One of the clear advantages of our approach is that it provides a new method to constrain the growth rate of structure. Consequently, it is informative to compare our results to those from other analyses of 6dFGS. Several RSD analyses have been performed using 6dFGS: [Beutler et al. \(2012\)](#) presented a traditional RSD analysis, [Achitouv et al. \(2016\)](#) looked at RSD in the void-galaxy cross-correlation, and [Blake et al. \(2018\)](#) presented a Fourier-space analysis using the RSD power spectrum multipoles. In addition to these, [Johnson et al. \(2014\)](#) and [Huterer et al. \(2017\)](#) both presented logarithmic distance ratio auto-covariance analyses using the 6dFGSv sample. Finally, [Qin et al. \(2019\)](#) applied a new estimator of the redshift-space density and momentum power spectra to redshifts and peculiar velocities from 6dFGSv.

Our galaxy overdensity auto-covariance analysis is most comparable to the results from [Beutler et al. \(2012\)](#). However, there are some minor differences that should be kept in mind. The galaxy overdensity sample used by [Beutler et al. \(2012\)](#) has a slightly lower magnitude cut ($K \leq 12.75$ compared to $K \leq 12.9$), and uses galaxies from a larger redshift range ($z \lesssim 0.2$), yielding 81,971 galaxies compared to the 70,467 galaxies used in our analysis. We also note that the [Beutler et al. \(2012\)](#) analysis employs the Feldman-Kaiser-Peacock (FKP; [Feldman et al. 1994](#)) weighting scheme to improve their statistical constraints, where we do not. By measuring the correlation function, they found $f\sigma_8 = 0.423 \pm 0.055$ (13% relative uncertainty) and $\beta = 0.373 \pm 0.054$ (14% relative uncertainty). These results are significantly better (although still consistent at the 1σ level) than our galaxy overdensity auto-covariance results of $f\sigma_8 = 0.41^{+0.15}_{-0.14}$ and $\beta = 0.30^{+0.13}_{-0.11}$. There are several factors that could explain this: [Beutler et al. \(2012\)](#) use a higher redshift sample, FKP weighting, and have access to smaller-scale information, which we lose by smoothing our model after gridding. We note that in terms of statistical uncertainties, our complete covariance constraints of $f\sigma_8 = 0.384 \pm 0.052$ and $\beta = 0.289^{+0.044}_{-0.043}$ are better than those from [Beutler et al. \(2012\)](#), although this advantage is lost when considering the combined statistical and systematic uncertainty.

As in this work, the analysis by [Achitouv et al. \(2016\)](#) also uses the [Beutler et al. \(2012\)](#) galaxy overdensity sample as a starting point. For their void-galaxy cross-correlation analysis, they take a volume-limited sample out to redshift $z = 0.05$, similar to the sample selection we made in our first analysis, and implement FKP weighting. They find $f\sigma_8 = 0.39 \pm 0.11$ when fitting to the void-galaxy cross-correlation

function, which is consistent with both our galaxy overdensity auto-covariance and complete covariance results at the 1σ level. Even with the lower redshift sample, this work provides a tighter constraint than our galaxy overdensity auto-covariance. We expect that the same factors that we highlighted when comparing to Beutler et al. (2012) are at play, especially the fact that the correlation fitting method may be accessing information on smaller scales.

Blake et al. (2018) presented an RSD analysis that fits to the power spectrum multipoles rather than the correlation function, making it the first Fourier-space analysis of RSD for 6dFGS. We note that they used the same sample as us: the Beutler et al. (2012) sample out to redshift $z = 0.1$, and they implement FKP weighting. They find $f\sigma_8 = 0.38 \pm 0.12$, which is consistent with both our galaxy overdensity auto-covariance and complete covariance results at the 1σ level. In their analysis, they highlighted that their larger statistical uncertainty (relative to the standard correlation function analysis from Beutler et al. 2012) was likely due to the correlation function analysis accessing smaller scale information than was available in the multipoles analysis. This is consistent with the interpretation of our own results, and this coupled with the fact that Blake et al. (2018) also used FKP weighting could explain why our statistical uncertainty is slightly larger than theirs but more than double that from Beutler et al. (2012).

Our method has been largely informed by that of Johnson et al. (2014), who effectively presented an logarithmic distance ratio auto-covariance analysis of 6dFGSv. They found $f\sigma_8 = 0.428^{+0.079}_{-0.068}$, which is consistent with our both our logarithmic distance ratio auto-covariance and complete covariance results at the 1σ level. We note that their constraint is better than our logarithmic distance ratio auto-covariance constraint of $f\sigma_8 = 0.53^{+0.11}_{-0.10}$. We suspect that this may be due to the fact that Johnson et al. (2014) used a gridding scale of $10 h^{-1}$ Mpc where we used $20 h^{-1}$ Mpc. This would result in more covariance entries and potentially lower the statistical uncertainty.

Huterer et al. (2017) performed a very similar analysis to Johnson et al. (2014) using 6dFGSv, but did not grid their sample. They found $f\sigma_8 = 0.481^{+0.067}_{-0.064}$, which is again consistent with our logarithmic distance ratio auto-covariance and complete covariance results at the 1σ level. We note that the lower absolute statistical uncertainty relative to Johnson et al. (2014) could be to do with the number of entries in the covariance matrix.

Finally, Qin et al. (2019) applied an estimator of the redshift-space density and momentum power spectra to 6dFGSv, constraining the growth rate of structure by comparing their estimated power spectra to modelled power spectra. This is similar to our work in that it utilises both redshifts and peculiar velocities, and while the methods are different, we consider them to be highly complementary. They found $f\sigma_8 = 0.451^{+0.108}_{-0.092}$, which is consistent with both of our auto-covariance results and the complete covariance result at the 1σ level.

We show a visual comparison of our $f\sigma_8$ constraints to these existing 6dFGS constraints in Fig. 12.

5.2.5 Density-Velocity Comparison Approaches

Density-velocity comparison approaches also take advantage of the shared information between the galaxy overdensity and peculiar velocity fields, albeit in a different way to our method. These methods use gravitational instability theory to relate the galaxy overdensity field to the peculiar velocity field through

$$v_p(\mathbf{r}) = \frac{H_0\beta}{4\pi} \int d^3\mathbf{r}' \frac{\delta_g(\mathbf{r}')(\mathbf{r}' - \mathbf{r})}{|\mathbf{r}' - \mathbf{r}|^3}. \quad (40)$$

This relation can be used to predict the peculiar velocity field from the observed galaxy overdensity field; comparing the modelled field to the observed field then allows one to constrain β . The growth rate can be extracted from this if one has an estimate of the galaxy bias for the sample.

The three studies we compare our results to are Pike & Hudson (2005), Davis et al. (2011) and Carrick et al. (2015). We note that all three use variations of the 2-Micron All-Sky Survey (2MASS) for the galaxy overdensity sample and variations of the Spiral Field I-Band survey for the velocity sample. Pike & Hudson (2005) found $f\sigma_8 = 0.44 \pm 0.06$, Davis et al. (2011) found $f\sigma_8 = 0.32 \pm 0.04$ and Carrick et al. (2015) found $f\sigma_8 = 0.427 \pm 0.027$. Our complete covariance constraints are consistent with each of these at the 1σ level, both with and without the systematic error, and our statistical uncertainty is between that of Pike & Hudson (2005) and Davis et al. (2011). We show a visual comparison of our complete covariance constraint for $f\sigma_8$ to these existing velocity-velocity constraints in Fig. 12.

5.2.6 Cross-Correlation Only Analysis

Finally, we compare our constraint of $f\sigma_8$ to that from Nusser (2017), who presented a fit to the cross-correlation function for galaxy overdensities (from 2MASS) and peculiar velocities (from the *cosmicflows-3* catalogue). This is more similar to the analysis by Achitouv et al. (2016) than our analysis in that they model the cross-correlation as a function of separation, similar to how Achitouv et al. (2016) modelled the cross-correlation function between galaxies and voids. They found $f\sigma_8 = 0.40 \pm 0.08$, which is consistent with our complete covariance constraint at the 1σ level. The construction of this method means they only utilise the equivalent of our cross-covariance, rather than the complete covariance. This explains why we see tighter statistical uncertainties. We show a visual comparison of our complete covariance constraint for $f\sigma_8$ to this constraint in Fig. 12.

5.3 Future Work

We now highlight possible improvements and new research opportunities that arise from this work.

In Section 3.3.4 we introduced α_b to parametrize the difference in the effective galaxy bias of the galaxy overdensity auto-correlation and cross-correlation. While we found that this parameter was sufficient to recover the growth rate of structure in the mocks, it was the dominant source of systematic uncertainty in our final constraints. This can be linked to the fact that α_b represents more than just the difference between effective bias values; it directly influences the amplitude of the cross-covariance, such that a

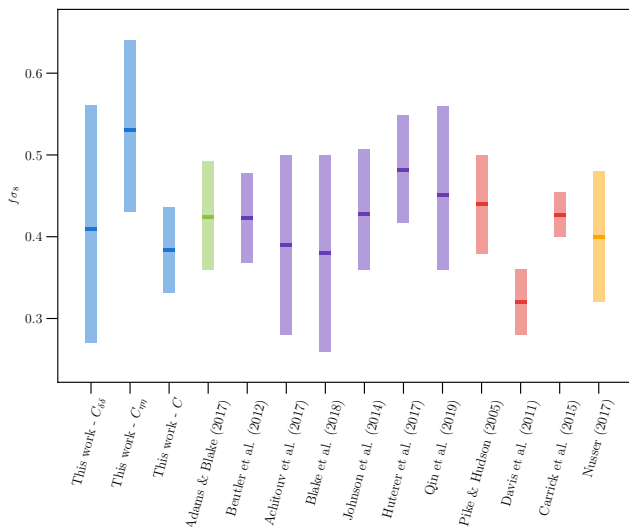


Figure 12. Median values (solid bar) and 68% credible interval (shaded region) of $f\sigma_8$ for this work (shown in blue) and Adams & Blake (2017) (shown in light green). Other works utilising 6dFGS are shown in purple, velocity-velocity comparisons are shown in red and the cross-correlation only analysis is shown in orange.

lower value of α_b may signify that the cross-correlation between peculiar velocities and galaxy overdensities is weaker than anticipated by our model. We discovered this behaviour when fitting our model with different values of α_b , noting that the posteriors on $f\sigma_8$ appeared to converge for increasingly small values of α_b (see Fig. 8).

Noting that the difference in effective bias arises from being unable to use a volume-limited sample, we can turn to work on the bias-luminosity relation for inspiration. For example, Beutler et al. (2013) characterised the bias-luminosity relation for 6dFGS; this could be used to modify the cross-correlation model to account for the expected galaxy bias when considering how a given peculiar velocity responds to a particular galaxy overdensity. An alternative would be to modify the data directly such that the galaxy overdensity sample had a constant galaxy bias over the whole volume, as implemented by Carrick et al. (2015). We believe significant further research is required to implement either of these solutions for our method, which includes validation with simulations before application to data.

While modelling redshift-space distortions, we have assumed that the parallel-plane approximation holds for our data. This approximation has been shown to break down for galaxy pairs with wide opening angles, which is common for large-area surveys at low-redshift, like 6dFGS. We note that redshift-space distortions may be modelled without this limit, as shown by Szalay et al. (1998) and Szapudi (2004), and that such modelling was included in the original 6dFGS redshift-space distortion analysis by Beutler et al. (2012). To our knowledge, the cross-correlation model has not been derived without assuming the parallel-plane approximation, which would need to be done before it could be adopted self-consistently into our model.

In terms of the redshift-space distortion model, we also note that Beutler et al. (2012) use Feldman-Kaiser-Peacock weighting to improve their constraints. Future work on the

covariance model could include an investigation into implementing the weighting scheme and its effect on our constraints.

Given that Johnson et al. (2014) provided scale-dependent constraints on the growth rate of structure for peculiar velocities using a similar model formalism, we believe implementing a similar capability for the complete covariance is a natural extension of this work. Based on the improvements we saw in the growth rate when including the cross-covariance, we expect similar improvements in constraints of the growth rate in scale-dependent bins. Tighter constraints would enable better tests of modified gravity models, such as those presented by Johnson et al. (2016).

Our method is also nicely set up to look for signatures left behind by non-Gaussian perturbations present during the inflationary period of the Universe. Such perturbations are a feature of alternative inflation models and they imprint a scale-dependent bias in the galaxy distribution. Consequently, any deviation from Gaussianity in the early universe modifies galaxy clustering on very large scales; the strength of the deviation is parametrized by f_{NL} . While large scales are difficult to measure in low-redshift surveys (making it difficult to constrain f_{NL}), adding peculiar velocities and their cross-correlation with the galaxy distribution may tighten such constraints. For example, Howlett et al. (2016) used Fisher matrix forecasts to show that the cross-correlation helps break degeneracies between f_{NL} and β , which improves constraints on f_{NL} by up to 40%. This has already been leveraged by Ma et al. (2013), who constrained f_{NL} in the local universe using a density-velocity comparison analysis, but it would also be possible to implement it within our modelling framework.

One of the major benefits of our method is that any model where the power spectrum is proportional to the growth rate of structure could be substituted. We could potentially use this feature to constrain the growth rate under the assumption of a specific modified gravity model (such as $f(R)$ gravity), rather than under the assumption of general relativity. This could be done by using power spectra for modified gravity models, such as those produced by MGCAMB (Hojjati et al. 2011). Such research would provide interesting insights into how growth rate of structure constraints respond to the assumed cosmological and gravitational model.

Finally, the upcoming Taipan Galaxy Survey (da Cunha et al. 2017) is set to improve the redshift and peculiar velocity samples significantly, leading to better constraints of the growth rate of structure.

6 SUMMARY

We have presented a significant advancement by adding redshift-space distortions (RSD) to the self-consistent model of the auto- and cross-covariance for the galaxy overdensity and peculiar velocity fields presented by Adams & Blake (2017). This has allowed us to directly test whether the same growth rate drives the amplitude of peculiar velocities and RSD. We have also performed a detailed analysis of how various model systematics affect our final growth rate constraint from 6dFGS and have provided a systematic error estimate in addition to our statistical uncertainty.

Our constraints from the complete covariance model are

$f\sigma_8 = 0.384 \pm 0.052(\text{stat}) \pm 0.061(\text{sys})$ for the growth rate of structure and $\beta = 0.289^{+0.044}_{-0.043}(\text{stat}) \pm 0.049(\text{sys})$ for the redshift-space distortion parameter. We found that the statistical uncertainties were reduced by 64% when compared to the galaxy overdensity auto-covariance only constraint and 50% when compared to the logarithmic distance ratio auto-covariance only constraint. Our current analysis provides an 18% improvement on the statistical uncertainty in $f\sigma_8$ found by Adams & Blake (2017). We believe this improvement is driven both by the improved model, which captures the information on the growth rate of structure encoded in the galaxy overdensity field through RSD, and by the use of a larger galaxy overdensity sample. The fact that our systematic uncertainties are larger than our statistical uncertainties is primarily driven by the degeneracy between the growth rate and the relative effective bias between the galaxy overdensity auto-covariance and cross-covariance, which we parametrized as α_b . We anticipate that this could be mitigated by improving our underlying bias model to account for the fact that the cross-covariance is sensitive to a different effective bias than the galaxy overdensity auto-covariance. We found that our constraint is consistent with the Λ CDM prediction of $f\sigma_8$ from the Planck 2015 cosmological parameters, as well as multiple analyses of galaxy overdensities and peculiar velocities from 6dFGS. This validates our method as a new approach for constraining $f\sigma_8$ from large-scale structure and peculiar velocities.

As in Adams & Blake (2017), we see obvious improvements in the statistical uncertainty when utilising the cross-covariance compared to either auto-covariance alone, or the naive constraint that one achieves by treating the two fields as independent. Once again, this supports the findings from the various theoretical studies on multi-tracer analyses, where accessing cross-correlations improves constraints. Our results also motivate the application of this method to future large-scale structure and peculiar velocity surveys such as Taipan.

ACKNOWLEDGEMENTS

We are thankful to the referee for providing a thoughtful and constructive review of our work. We are grateful to Paul Carter and Florian Beutler for providing the 6dFGS COLA mocks we employed in this paper. The 6dF Galaxy Survey was made possible by contributions from many individuals towards the instrument, the survey and its science. We particularly thank Matthew Colless, Heath Jones, Will Saunders, Fred Watson, Quentin Parker, Mike Read, Lachlan Campbell, Chris Springob, Christina Magoulas, John Lucey, Jeremy Mould, and Tom Jarrett, as well as the dedicated staff of the Australian Astronomical Observatory and other members of the 6dFGS team over the years. We have used `matplotlib` (Hunter 2007) for the generation of scientific plots. This research was conducted by the Australian Research Council Centre of Excellence for All-sky Astrophysics (CAASTRO), through project number CE110001020. CA was supported by an Australian Government Research Training Program Scholarship.

REFERENCES

- Abate A., Bridle S., Teodoro L. F. A., Warren M. S., Hendry M., 2008, *Monthly Notices of the Royal Astronomical Society*, 389, 1739
- Abramo L. R., Leonard K. E., 2013, *Monthly Notices of the Royal Astronomical Society*, 432, 318
- Achitouv I., Blake C., Carter P., Koda J., Beutler F., 2016, *Physical Review D*, 95, 083502
- Adams C., Blake C., 2017, *Monthly Notices of the Royal Astronomical Society*, 471, 839
- Alam S., et al., 2017, *Monthly Notices of the Royal Astronomical Society*, 470, 2617
- Ata M., et al., 2018, *Monthly Notices of the Royal Astronomical Society*, 473, 4773
- Bernstein G. M., Cai Y. C., 2011, *Monthly Notices of the Royal Astronomical Society*, 416, 3009
- Beutler F., et al., 2011, *Monthly Notices of the Royal Astronomical Society*, 416, 3017
- Beutler F., et al., 2012, *Monthly Notices of the Royal Astronomical Society*, 423, 3430
- Beutler F., et al., 2013, *Monthly Notices of the Royal Astronomical Society*, 429, 3604
- Blake C., et al., 2011, *Monthly Notices of the Royal Astronomical Society*, 415, 2876
- Blake C., et al., 2013, *Monthly Notices of the Royal Astronomical Society*, 436, 3089
- Blake C., Carter P., Koda J., 2018, *Monthly Notices of the Royal Astronomical Society*, 479, 5168
- Burkey D., Taylor A. N., 2004, *Monthly Notices of the Royal Astronomical Society*, 347, 255
- Burnham K. P., Anderson D. R., 2004, *Model Selection and Multimodel Inference*. Springer New York, New York, NY ([arXiv:1011.1669v3](https://arxiv.org/abs/1011.1669v3)), doi:10.1007/b97636, <http://link.springer.com/10.1007/b97636>
- Carrick J., Turnbull S. J., Lavaux G., Hudson M. J., 2015, *Monthly Notices of the Royal Astronomical Society*, 450, 317
- Carter P., Beutler F., Percival W. J., Blake C., Koda J., Ross A. J., 2018, *Monthly Notices of the Royal Astronomical Society*, 481, 2371
- Crocce M., Scoccimarro R., Bernardeau F., 2012, *Monthly Notices of the Royal Astronomical Society*, 427, 2537
- Davis M., Nusser A., Masters K. L., Springob C., Huchra J. P., Lemson G., 2011, *Monthly Notices of the Royal Astronomical Society*, 413, 2906
- Dekel A., Lahav O., 1999, *The Astrophysical Journal*, 520, 24
- Desjacques V., Sheth R. K., 2010, *Physical Review D - Particles, Fields, Gravitation and Cosmology*, 81, 023526
- Feldman H. A., Kaiser N., Peacock J. A., 1994, *The Astrophysical Journal*, 426, 23
- Foreman-Mackey D., Hogg D. W., Lang D., Goodman J., 2013, *Publications of the Astronomical Society of the Pacific*, 125, 306
- Gelman A., Rubin D. B., 1992, *Statistical Science*, 7, 457
- Gil-Marín H., Wagner C., Verde L., Jimenez R., Heavens A. F., 2010, *Monthly Notices of the Royal Astronomical Society*, 407, 772
- Goodman J., Weare J., 2010, *Communications in Applied Mathematics and Computational Science*, 5, 65
- Hinton S., 2016, *The Journal of Open Source Software*, 1, 45
- Hojjati A., Pogosian L., Zhao G.-B., 2011, *Journal of Cosmology and Astroparticle Physics*, 2011, 005
- Howlett C., Staveley-Smith L., Blake C., 2016, *Monthly Notices of the Royal Astronomical Society*, 464, 2517
- Hui L., Greene P. B., 2006, *Physical Review D*, 73, 123526
- Hunter J. D., 2007, *Computing in Science and Engineering*, 9, 99
- Huterer D., Shafer D. L., Scolnic D. M., Schmidt F., 2017, *Journal of Cosmology and Astroparticle Physics*, 2017, 015

- Johnson A., et al., 2014, *Monthly Notices of the Royal Astronomical Society*, 444, 3926
- Johnson A., Blake C., Dossett J., Koda J., Parkinson D., Joudaki S., 2016, *Monthly Notices of the Royal Astronomical Society*, 458, 2725
- Jones D. H., Saunders W., Read M., Colless M., 2005, *Publications of the Astronomical Society of Australia*, 22, 277
- Jones D. H., Peterson B. A., Colless M., Saunders W., 2006, *Monthly Notices of the Royal Astronomical Society*, 369, 25
- Jones D. H., et al., 2009, *Monthly Notices of the Royal Astronomical Society*, 399, 683
- Kaiser N., 1987, *Monthly Notices of the Royal Astronomical Society*, 227, 1
- Koda J., et al., 2014, *Monthly Notices of the Royal Astronomical Society*, 445, 4267
- Komatsu E., et al., 2009, *Astrophysical Journal, Supplement Series*, 180, 330
- Lewis A., Challinor A., 2011, *Astrophysics Source Code Library*
- Lewis A., Challinor A., Lasenby A., 2000, *The Astrophysical Journal*, 538, 473
- Linder E. V., 2005, *Physical Review D*, 72, 043529
- Ma Y.-Z., Taylor J. E., Scott D., 2013, *Monthly Notices of the Royal Astronomical Society*, 436, 2029
- Magoulas C., et al., 2012, *Monthly Notices of the Royal Astronomical Society*, 427, 245
- McDonald P., Seljak U., 2009, *Journal of Cosmology and Astroparticle Physics*, 2009, 007
- Nusser A., 2017, *Monthly Notices of the Royal Astronomical Society*, 470, 445
- Peacock J. A., Dodds S. J., 1994, *Monthly Notices of the Royal Astronomical Society*, 267, 1020
- Peacock J. A., et al., 2001, *Nature*, 410, 169
- Pike R. W., Hudson M. J., 2005, *The Astrophysical Journal*, 635, 11
- Planck Collaboration et al., 2015, *Astronomy & Astrophysics*, 594, A13
- Planck Collaboration et al., 2018, preprint ([arXiv:1807.06209](https://arxiv.org/abs/1807.06209))
- Qin F., Howlett C., Staveley-Smith L., 2019, *Monthly Notices of the Royal Astronomical Society*, 487, 5235
- Ruggeri R., et al., 2019, *Monthly Notices of the Royal Astronomical Society*, 483, 3878
- Scolnic D. M., et al., 2017, *The Astrophysical Journal*, 859, 101
- Springob C. M., et al., 2014, *Monthly Notices of the Royal Astronomical Society*, 445, 2677
- Szalay A. S., Matsubara T., Landy S. D., 1998, *The Astrophysical Journal*, 498, L1
- Szapudi I., 2004, *The Astrophysical Journal*, 614, 51
- Tassev S., Zaldarriaga M., Eisenstein D. J., 2013, *Journal of Cosmology and Astroparticle Physics*, 2013, 036
- Zhang B. R., Childress M. J., Davis T. M., Karpenka N. V., Lidman C., Schmidt B. P., Smith M., 2017, *Monthly Notices of the Royal Astronomical Society*, 471, 2254
- da Cunha E., et al., 2017, *Publications of the Astronomical Society of Australia*, 34, e047

APPENDIX A: DERIVATION OF COVARIANCE EXPRESSIONS UNDER RSD

In this Appendix, we present the derivation of the expressions for the four covariance matrices that make up our complete model covariance, defined as

$$\mathbf{C} = \begin{pmatrix} \mathbf{C}_{\delta\delta} & \mathbf{C}_{\delta\eta} \\ \mathbf{C}_{\eta\delta} & \mathbf{C}_{\eta\eta} \end{pmatrix}, \quad (\text{A1})$$

where $\mathbf{C}_{\delta\delta}$ is the galaxy overdensity auto-covariance, $\mathbf{C}_{\eta\eta}$ is the logarithmic distance ratio auto-covariance, and $\mathbf{C}_{\delta\eta}$

and $\mathbf{C}_{\eta\delta}$ are the cross-covariances. This model corresponds to our chosen data vector

$$\mathbf{\Delta} = \begin{pmatrix} \delta \\ \eta \end{pmatrix}, \quad (\text{A2})$$

where $\mathbf{\Delta}$ contains the list of overdensities δ_g and logarithmic distance ratios η measured from simulations or the 6-degree Field Galaxy Survey. In this appendix, we will present the model for peculiar velocity, which is related to the logarithmic distance ratio via the conversion factor ξ , defined in Eq. 20.

As we are modelling the effects of redshift-space distortions (RSD), our theoretical model for the galaxy overdensity in Fourier space is

$$\tilde{\delta}_g^s(\mathbf{k}) = [b\tilde{\delta}_m(\mathbf{k}) + f\mu^2\tilde{\theta}(\mathbf{k})]D_g(k, \mu, \sigma_g), \quad (\text{A3})$$

and our theoretical model for the logarithmic distance ratio is

$$\tilde{v}_p(\mathbf{k}) = -iaHf\frac{\mu}{k}\tilde{\theta}(\mathbf{k})D_u(k, \sigma_u). \quad (\text{A4})$$

Here, $\tilde{\delta}_m(\mathbf{k})$ is the matter overdensity field and $\tilde{\theta}(\mathbf{k})$ is the velocity divergence field, both in Fourier space. b is the galaxy bias in real space, f is the growth rate of structure, a is the cosmological scale factor, and H is the Hubble parameter. D_g and D_u are the damping functions for the RSD model, defined in terms of their respective damping parameters (σ_g and σ_u) in Eq. 4 and 6.

Throughout, we use the following position conventions:

$$\mathbf{x}_s = (x_{sx}, x_{sy}, x_{sz}), \quad |\mathbf{x}_s| = x_s, \quad (\text{A5})$$

$$\mathbf{x}_t = (x_{tx}, x_{ty}, x_{tz}), \quad |\mathbf{x}_t| = x_t, \quad (\text{A6})$$

$$\mathbf{r} = \mathbf{x}_t - \mathbf{x}_s = (r_x, r_y, r_z), \quad |\mathbf{r}| = r, \quad (\text{A7})$$

$$\mathbf{d} = \frac{1}{2}[\mathbf{x}_t + \mathbf{x}_s] = (d_x, d_y, d_z), \quad |\mathbf{d}| = d, \quad (\text{A8})$$

$$\hat{\mathbf{k}} = (\sin\theta\cos\phi, \sin\theta\sin\phi, \cos\theta), \quad (\text{A9})$$

$$\mu = \hat{\mathbf{k}} \cdot \hat{\mathbf{d}}. \quad (\text{A10})$$

We refer the reader to fig. 2 of [Adams & Blake \(2017\)](#) for a visual representation of the configuration space vectors and angles.

Eq. A3 and A4 allow us to calculate the anisotropic power spectra:

$$P_{gg}(k, \mu) = b^2[P_{mm}(k) + 2r_g\beta\mu^2P_{m\theta}(k) + \beta^2\mu^4P_{\theta\theta}(k)]D_g^2(k, \mu, \sigma_g), \quad (\text{A11})$$

$$P_{gv}(k, \mu) = \frac{iaHfb\mu}{k}[r_gP_{m\theta}(k) + \beta\mu^2P_{\theta\theta}(k)]D_g(k, \mu, \sigma_g)D_u(k, \sigma_u), \quad (\text{A12})$$

$$P_{vg}(k, \mu) = \frac{-iaHfb\mu}{k}[r_gP_{m\theta}(k) + \beta\mu^2P_{\theta\theta}(k)]D_g(k, \mu, \sigma_g)D_u(k, \sigma_u), \quad (\text{A13})$$

$$P_{vv}(k, \mu) = \left(\frac{aHf\mu}{k}\right)^2 P_{\theta\theta}(k)D_u^2(k, \sigma_u), \quad (\text{A14})$$

where r_g is the cross-correlation coefficient discussed in the text following Eq. 10.

Throughout the following sections, we use a number of mathematical identities and definitions. Given we are working with anisotropic power spectra, we make use of the mul-

tipole expansion

$$P(k, \mu) = \sum_{\ell=0}^{\infty} P_{\ell}(k) L_{\ell}(\mu), \quad (\text{A15})$$

where $P_{\ell}(k)$ are the multipole power spectra and $L_{\ell}(\mu)$ are the Legendre polynomials. Eq. A15 can then be evaluated for the required P_{ℓ} , which is done by multiplying each side by $L_{\ell'}(\mu)$ and taking advantage of the normalisation condition for Legendre polynomials:

$$\int_{-1}^1 L_{\ell}(x) L_{\ell'}(x) dx = \frac{2}{2\ell' + 1} \delta_{\ell\ell'}, \quad (\text{A16})$$

such that

$$P_{\ell}(k) = \int_{-1}^1 \frac{2\ell + 1}{2} L_{\ell}(\mu) P(k, \mu) d\mu. \quad (\text{A17})$$

The expression of the wavevector in spherical coordinates allows us to utilise the plane wave expansion

$$e^{i\mathbf{k} \cdot \mathbf{r}} = \sum_{\ell} i^{\ell} (2\ell + 1) j_{\ell}(kr) L_{\ell}(\hat{\mathbf{k}} \cdot \hat{\mathbf{r}}), \quad (\text{A18})$$

where j_{ℓ} are the spherical Bessel functions and L_{ℓ} are the Legendre polynomials. It is also useful to note that any function of θ and ϕ may be expressed as a linear sum of spherical harmonic functions:

$$f(\theta, \phi) = \sum_{\ell=0}^{\infty} \sum_{m=-\ell}^{\ell} f_{\ell m} Y_{\ell m}(\theta, \phi), \quad (\text{A19})$$

and that the coefficients can be directly calculated through

$$f_{\ell m} = \int_{\theta=0}^{\pi} \int_{\phi=0}^{2\pi} f(\theta, \phi) Y_{\ell m}^*(\theta, \phi) \sin(\theta) d\theta d\phi. \quad (\text{A20})$$

We also note that our normalisation convention for spherical harmonics is such that we may define the complex conjugate of $Y_{\ell m}(\theta, \phi)$ to be

$$Y_{\ell m}^*(\theta, \phi) = (-1)^m Y_{\ell, -m}(\theta, \phi), \quad (\text{A21})$$

and that the following orthonormal condition holds:

$$\int_{\theta=0}^{\pi} \int_{\phi=0}^{2\pi} Y_{\ell m}(\theta, \phi) Y_{\ell' m'}^*(\theta, \phi) \sin(\theta) d\theta d\phi = \delta_{\ell\ell'} \delta_{m m'}, \quad (\text{A22})$$

where $\delta_{\ell\ell'}$ and $\delta_{m m'}$ are Kronecker delta functions, which evaluate to 1 if the subscripts are equal and 0 otherwise. Finally, we note that the spherical harmonic addition theorem is useful when working with Legendre polynomials where the argument is a dot-product of unit vectors:

$$\begin{aligned} L_{\ell}(\hat{\mathbf{k}} \cdot \hat{\mathbf{r}}) &= \frac{4\pi}{(2\ell + 1)} \sum_{m=-\ell}^{\ell} Y_{\ell m}(\hat{\mathbf{k}}) Y_{\ell m}(\hat{\mathbf{r}})^* \\ &= \frac{4\pi}{(2\ell + 1)} \sum_{m=-\ell}^{\ell} Y_{\ell m}(\hat{\mathbf{k}})^* Y_{\ell m}(\hat{\mathbf{r}}). \end{aligned} \quad (\text{A23})$$

A1 Galaxy Overdensity Auto-Covariance

Given the definition of the anisotropic power spectrum, we can write the galaxy overdensity auto-covariance as

$$C_{\delta\delta}(\mathbf{x}_s, \mathbf{x}_t) = \frac{1}{(2\pi)^3} \int P_{gg}(k, \mu) e^{i\mathbf{k} \cdot \mathbf{r}} d^3 \mathbf{k}. \quad (\text{A24})$$

Utilising Eq. A15 and A18:

$$C_{\delta\delta}(\mathbf{x}_s, \mathbf{x}_t) = \frac{1}{(2\pi)^3} \int \sum_{\ell, \ell'} P_{gg, \ell}(k) L_{\ell}(\hat{\mathbf{k}} \cdot \hat{\mathbf{d}}) (2\ell' + 1) i^{\ell'} j_{\ell'}(kr) L_{\ell'}(\hat{\mathbf{k}} \cdot \hat{\mathbf{r}}) d^3 \mathbf{k}. \quad (\text{A25})$$

This can then be expanded through the spherical harmonic addition theorem (Eq. A23):

$$\begin{aligned} C_{\delta\delta}(\mathbf{x}_s, \mathbf{x}_t) &= \frac{1}{(2\pi)^3} \int \sum_{\ell, \ell'} \sum_{m, m'} P_{gg, \ell}(k) \frac{4\pi}{(2\ell + 1)} \\ &\quad Y_{\ell m}(\hat{\mathbf{k}}) Y_{\ell m}^*(\hat{\mathbf{d}}) (2\ell' + 1) i^{\ell'} j_{\ell'}(kr) \\ &\quad \frac{4\pi}{(2\ell' + 1)} Y_{\ell' m'}^*(\hat{\mathbf{k}}) Y_{\ell' m'}(\hat{\mathbf{r}}) d^3 \mathbf{k}. \end{aligned} \quad (\text{A26})$$

We now break up the integral into spherical coordinates $d^3 \mathbf{k} = k^2 \sin(\theta) d\phi d\theta dk$, noting that $\hat{\mathbf{k}}$ is a function of θ and ϕ , but $\hat{\mathbf{d}}$ and $\hat{\mathbf{r}}$ are not. This allows us to group the spherical harmonic functions into configuration-space and Fourier-space pairs:

$$\begin{aligned} C_{\delta\delta}(\mathbf{x}_s, \mathbf{x}_t) &= \frac{1}{(2\pi)^3} \int_0^{\infty} \sum_{\ell, \ell'} \sum_{m, m'} k^2 P_{gg, \ell}(k) \frac{(4\pi)^2}{(2\ell + 1)} \\ &\quad Y_{\ell m}^*(\hat{\mathbf{d}}) Y_{\ell' m'}(\hat{\mathbf{r}}) i^{\ell'} j_{\ell'}(kr) \\ &\quad \int_0^{\pi} \int_0^{2\pi} Y_{\ell m}(\hat{\mathbf{k}}) Y_{\ell' m'}^*(\hat{\mathbf{k}}) \\ &\quad \sin(\theta) d\phi d\theta dk. \end{aligned} \quad (\text{A27})$$

The angular integral corresponds to the orthonormal condition of spherical harmonics (Eq. A22), producing the pair of delta functions $\delta_{\ell\ell'} \delta_{m m'}$ such that

$$\begin{aligned} C_{\delta\delta}(\mathbf{x}_s, \mathbf{x}_t) &= \frac{1}{(2\pi)^3} \int_0^{\infty} \sum_{\ell} \sum_m k^2 P_{gg, \ell}(k) \frac{(4\pi)^2}{(2\ell + 1)} \\ &\quad Y_{\ell m}^*(\hat{\mathbf{d}}) Y_{\ell m}(\hat{\mathbf{r}}) i^{\ell} j_{\ell}(kr) dk, \end{aligned} \quad (\text{A28})$$

which can be further reduced through the spherical harmonic addition theorem to

$$C_{\delta\delta}(\mathbf{x}_s, \mathbf{x}_t) = \frac{1}{2\pi^2} \int_0^{\infty} \sum_{\ell} k^2 P_{gg, \ell}(k) L_{\ell}(\cos \gamma) i^{\ell} j_{\ell}(kr) dk \quad (\text{A29})$$

where γ is the angle between \mathbf{r} and \mathbf{d} .

The next step is to assess which values of ℓ are required for the expansion, and to determine the power spectrum multipole function at the required ℓ . Given the form of the expansion (Eq. A15), the required values of ℓ are determined by the orders of μ that appear in the anisotropic power spectrum. For the galaxy-galaxy anisotropic power spectrum (Eq. A11), the orders of μ are 0, 2, 4. Recalling the definition of the power spectrum multipoles (Eq. A17):

$$\begin{aligned} P_{gg, \ell}(k) &= \int_{-1}^1 \frac{2\ell + 1}{2} L_{\ell}(\mu) b^2 [P_{mm}(k) + 2r_g \beta \mu^2 P_{m\theta}(k) + \\ &\quad \beta^2 \mu^4 P_{\theta\theta}(k)] D_g^2(k, \mu, \sigma_g) d\mu. \end{aligned} \quad (\text{A30})$$

As discussed in Section 3.2, we break the covariance into components that can be scaled by our free parameters, which saves computing time. The galaxy overdensity auto-covariance (given by Eq. A29 and A30) can be expressed

as

$$\mathbf{C}_{\delta\delta} = \frac{b^2}{2\pi^2} (\mathbf{C}_{\delta\delta,\beta^0} + 2r_g\beta\mathbf{C}_{\delta\delta,\beta^1} + \beta^2\mathbf{C}_{\delta\delta,\beta^2}), \quad (\text{A31})$$

where each of these covariance matrices will include the sum over ℓ of the power spectrum multipoles as well as the integrals over μ and k . The integral over μ can be evaluated analytically, whereas the integral over k is done numerically. We obtained the analytic expressions for the various covariances through **Mathematica**.

The covariances matrices for each order of β may then be expressed as the sum of integrand matrices for each value of ℓ , which we label with \mathbf{K} . For the β^0 term:

$$\mathbf{C}_{\delta\delta,\beta^0} = \int k^2 P_{mm}(k) \left[\mathbf{K}_{\delta\delta,\beta^0,\ell=0} + \mathbf{K}_{\delta\delta,\beta^0,\ell=2} + \mathbf{K}_{\delta\delta,\beta^0,\ell=4} \right] dk. \quad (\text{A32})$$

For a pair of positions (described by γ and r) the integrands have the following functional forms:

$$K_{\delta\delta,\beta^0,\ell=0} = \frac{1}{2k\sigma_g} \sqrt{\pi} \text{Erf}(k\sigma_g) j_0(kr), \quad (\text{A33})$$

$$K_{\delta\delta,\beta^0,\ell=2} = \frac{5}{8k^3\sigma_g^3} L_2(\cos\gamma) \left[6e^{-k^2\sigma_g^2} k\sigma_g + (-3 + 2k^2\sigma_g^2) \sqrt{\pi} \text{Erf}(k\sigma_g) \right] j_2(kr), \quad (\text{A34})$$

$$K_{\delta\delta,\beta^0,\ell=4} = \frac{9}{64k^5\sigma_g^5} L_4(\cos\gamma) \left[-10e^{-k^2\sigma_g^2} k\sigma_g (21 + 2k^2\sigma_g^2) + 3(35 - 20k^2\sigma_g^2 + 4k^4\sigma_g^4) \sqrt{\pi} \text{Erf}(k\sigma_g) \right] j_4(kr), \quad (\text{A35})$$

where $\text{Erf}(x)$ is the error function. For the β^1 term:

$$\mathbf{C}_{\delta\delta,\beta^1} = \int k^2 P_{mm}(k) \left[\mathbf{K}_{\delta\delta,\beta^1,\ell=0} + \mathbf{K}_{\delta\delta,\beta^1,\ell=2} + \mathbf{K}_{\delta\delta,\beta^1,\ell=4} \right] dk, \quad (\text{A36})$$

where

$$K_{\delta\delta,\beta^1,\ell=0} = \frac{1}{2k^3\sigma_g^3} \left[-2e^{-k^2\sigma_g^2} k\sigma_g + \sqrt{\pi} \text{Erf}(k\sigma_g) \right] j_0(kr), \quad (\text{A37})$$

$$K_{\delta\delta,\beta^1,\ell=2} = \frac{5}{8k^5\sigma_g^5} L_2(\cos\gamma) \left[2e^{-k^2\sigma_g^2} k\sigma_g (9 + 4k^2\sigma_g^2) + (-9 + 2k^2\sigma_g^2) \sqrt{\pi} \text{Erf}(k\sigma_g) \right] j_2(kr), \quad (\text{A38})$$

$$K_{\delta\delta,\beta^1,\ell=4} = \frac{-9}{64k^7\sigma_g^7} L_4(\cos\gamma) \left[2e^{-k^2\sigma_g^2} k\sigma_g (525 + 170k^2\sigma_g^2 + 32k^4\sigma_g^4) - 3(175 - 60k^2\sigma_g^2 + 4k^4\sigma_g^4) \sqrt{\pi} \text{Erf}(k\sigma_g) \right] j_4(kr). \quad (\text{A39})$$

Finally, the β^2 term can be expressed as:

$$\mathbf{C}_{\delta\delta,\beta^2} = \int k^2 P_{mm}(k) \left[\mathbf{K}_{\delta\delta,\beta^2,\ell=0} + \mathbf{K}_{\delta\delta,\beta^2,\ell=2} + \mathbf{K}_{\delta\delta,\beta^2,\ell=4} \right] dk, \quad (\text{A40})$$

where

$$K_{\delta\delta,\beta^2,\ell=0} = \frac{1}{8k^5\sigma_g^5} \left[-2e^{-k^2\sigma_g^2} k\sigma_g (3 + 2k^2\sigma_g^2) + 3\sqrt{\pi} \text{Erf}(k\sigma_g) \right] j_0(kr), \quad (\text{A41})$$

$$K_{\delta\delta,\beta^2,\ell=2} = \frac{5}{32k^7\sigma_g^7} L_2(\cos\gamma) \left[2e^{-k^2\sigma_g^2} k\sigma_g (45 + 24k^2\sigma_g^2 + 8k^4\sigma_g^4) + 3(-15 + 2k^2\sigma_g^2) \sqrt{\pi} \text{Erf}(k\sigma_g) \right] j_2(kr), \quad (\text{A42})$$

$$K_{\delta\delta,\beta^2,\ell=4} = \frac{-9}{256k^9\sigma_g^9} L_4(\cos\gamma) \left[2e^{-k^2\sigma_g^2} k\sigma_g (3675 + 1550k^2\sigma_g^2 + 416k^4\sigma_g^4 + 64k^6\sigma_g^6) - 3(1225 - 300k^2\sigma_g^2 + 12k^4\sigma_g^4) \sqrt{\pi} \text{Erf}(k\sigma_g) \right] j_4(kr). \quad (\text{A43})$$

A2 Peculiar Velocity Auto-Covariance

The mathematics for the peculiar velocity auto-covariance is largely the same as what we used in the previous section. Elements of the covariance matrix have the same form as Eq. A29:

$$C_{vv}(\mathbf{x}_s, \mathbf{x}_t) = \frac{1}{2\pi^2} \int_0^\infty \sum_\ell k^2 P_{vv,\ell}(k) L_\ell(\cos\gamma) i^\ell j_\ell(kr) dk, \quad (\text{A44})$$

where the multipole power spectra are given by

$$P_{vv,\ell}(k) = \int_{-1}^1 \frac{2\ell+1}{2} L_\ell(\mu) \left(\frac{aHf\mu}{k} \right)^2 P_{\theta\theta}(k) D_u^2(k, \sigma_u) d\mu. \quad (\text{A45})$$

For the velocity-velocity anisotropic power spectrum (Eq. A14), the orders of μ indicate that we require $\ell = 0, 2$ for the multipole expansion.

Unlike the galaxy overdensity auto-covariance, there is only a single order of β , so we do not need to express the total covariance as a sum over orders of β , as in Eq. A31. Instead, we may jump straight to the expression in terms of integrand matrices \mathbf{K} :

$$\mathbf{C}_{vv} = \frac{(aHf)^2}{2\pi^2} \int P_{\theta\theta}(k) D_u^2(k, \sigma_u) \left[\mathbf{K}_{vv,\ell=0} + \mathbf{K}_{vv,\ell=2} \right] dk. \quad (\text{A46})$$

For a pair of positions (described by γ and r) the integrands have the following functional forms:

$$K_{vv,\ell=0} = \frac{1}{3} j_0(kr) \quad (\text{A47})$$

$$K_{vv,\ell=2} = -\frac{2}{3} L_2(\cos\gamma) j_2(kr). \quad (\text{A48})$$

A3 Cross-Covariance

Again, the mathematics for introducing RSD to the cross-covariance is largely the same as that used in the previous derivations. Elements of the covariance matrix have the same form as Eq. A29:

$$\begin{aligned} C_{\delta v}(\mathbf{x}_\delta, \mathbf{x}_v) &= C_{v\delta}(\mathbf{x}_v, \mathbf{x}_\delta) \\ &= \frac{1}{2\pi^2} \int_0^\infty \sum_\ell k^2 P_{vg,\ell}(k) L_\ell(\cos \gamma) i^\ell j_\ell(kr) dk. \end{aligned} \quad (\text{A49})$$

Here, we have specified the equation in terms of the overdensity and velocity positions $(\mathbf{x}_\delta, \mathbf{x}_v)$. By choosing to define $\mathbf{r} = \mathbf{x}_\delta - \mathbf{x}_v$, we account for the asymmetry of the cross-covariance, which appears as a sign difference when working in terms of fixed positions $(\mathbf{x}_s, \mathbf{x}_t)$. Given there are outstanding factors of i , we note that the covariance expression above will only have the correct sign if calculated using the expression for $P_{vg,\ell}$.

The multipole power spectra are given by

$$\begin{aligned} P_{vg,\ell}(k) &= \int_{-1}^1 \frac{2\ell+1}{2} L_\ell(\mu) \frac{-iaHfb\mu}{k} [r_g P_{m\theta}(k) \\ &\quad + \beta \mu^2 P_{\theta\theta}(k)] D_u(k, \sigma_u) D_g(k, \mu, \sigma_g) d\mu. \end{aligned} \quad (\text{A51})$$

The orders of μ indicate that we require $\ell = 1, 3$ for the multipole expansion.

As with the galaxy overdensity auto-covariance, there are multiple orders of β , so we break up the covariance equation similarly to Eq. A52:

$$\mathbf{C}_{v\delta} = \frac{aHfb}{2\pi^2} (r_g \mathbf{C}_{v\delta,\beta^0} + \beta \mathbf{C}_{v\delta,\beta^1}). \quad (\text{A52})$$

Again, we obtain the analytic expressions for the various covariances through **Mathematica**.

The covariance matrices for each order of β may be expressed as the sum of integrand matrices for each value of ℓ , which we label with \mathbf{K} . For the β^0 term:

$$\mathbf{C}_{v\delta,\beta^0} = \int k P_{\theta m}(k) D_u(k, \sigma_u) \left[\mathbf{K}_{v\delta,\beta^0,\ell=1} + \mathbf{K}_{v\delta,\beta^0,\ell=3} \right] dk. \quad (\text{A53})$$

For a pair of positions (described by γ and r) the integrands have the following functional forms:

$$\begin{aligned} K_{v\delta,\beta^0,\ell=1} &= \frac{3}{2k^3 \sigma_g^3} L_1(\cos \gamma) \left[-2e^{-k^2 \sigma_g^2/2} k \sigma_g \right. \\ &\quad \left. + \sqrt{2\pi} \text{Erf} \left(\frac{k \sigma_g}{\sqrt{2}} \right) \right] j_1(kr), \end{aligned} \quad (\text{A54})$$

$$\begin{aligned} K_{v\delta,\beta^0,\ell=3} &= \frac{7}{4k^5 \sigma_g^5} L_3(\cos \gamma) \left[2e^{-k^2 \sigma_g^2/2} k \sigma_g (15 + 2k^2 \sigma_g^2) \right. \\ &\quad \left. + 3\sqrt{2\pi} (-5 + k^2 \sigma_g^2) \text{Erf} \left(\frac{k \sigma_g}{\sqrt{2}} \right) \right] j_3(kr), \end{aligned} \quad (\text{A55})$$

where $\text{Erf}(x)$ is the error function. For the β^1 term:

$$\mathbf{C}_{v\delta,\beta^1} = \int k P_{\theta m}(k) D_u(k, \sigma_u) \left[\mathbf{K}_{v\delta,\beta^1,\ell=1} + \mathbf{K}_{v\delta,\beta^1,\ell=3} \right] dk, \quad (\text{A56})$$

where

$$\begin{aligned} K_{v\delta,\beta^1,\ell=1} &= \frac{3}{2k^5 \sigma_g^5} L_1(\cos \gamma) \left[-2e^{-k^2 \sigma_g^2/2} k \sigma_g (3 + k^2 \sigma_g^2) \right. \\ &\quad \left. + 3\sqrt{2\pi} \text{Erf} \left(\frac{k \sigma_g}{\sqrt{2}} \right) \right] j_1(kr), \end{aligned} \quad (\text{A57})$$

$$\begin{aligned} K_{v\delta,\beta^1,\ell=3} &= \frac{7}{4k^7 \sigma_g^7} L_3(\cos \gamma) \left[2e^{-k^2 \sigma_g^2/2} k \sigma_g \right. \\ &\quad \left. (75 + 16k^2 \sigma_g^2 + 2k^4 \sigma_g^4) \right. \\ &\quad \left. + 3\sqrt{2\pi} (-25 + 3k^2 \sigma_g^2) \text{Erf} \left(\frac{k \sigma_g}{\sqrt{2}} \right) \right] j_3(kr). \end{aligned} \quad (\text{A58})$$

This paper has been typeset from a $\text{\TeX}/\text{\LaTeX}$ file prepared by the author.